THE HABITABLE ZONE OF EARTH-LIKE PLANETS WITH DIFFERENT LEVELS OF ATMOSPHERIC PRESSURE

GIOVANNI VLADILO[1,2], GIUSEPPE MURANTE[1], LAURA SILVA[1], ANTONELLO PROVENZALE[3],
GAIA FERRI[2], AND GREGORIO RAGAZZINI[2]
[1] INAF-Trieste Astronomical Observatory, Trieste, Italy; vladilo@oats.inaf.it
[2] Department of Physics, University of Trieste, Trieste, Italy
[3] Institute of Atmospheric Sciences and Climate-CNR, Torino, Italy

ABSTRACT

As a contribution to the study of the habitability of extrasolar planets, we implemented a one-dimensional energy balance model (EBM), the simplest seasonal model of planetary climate, with new prescriptions for most physical quantities. Here we apply our EBM to investigate the surface habitability of planets with an Earth-like atmospheric composition but different levels of surface pressure. The habitability, defined as the mean fraction of the planet's surface on which liquid water could exist, is estimated from the pressure-dependent liquid water temperature range, taking into account seasonal and latitudinal variations of surface temperature. By running several thousands of EBM simulations we generated a map of the habitable zone (HZ) in the plane of the orbital semi-major axis, a, and surface pressure, p, for planets in circular orbits around a Sun-like star. As pressure increases, the HZ becomes broader, with an increase of 0.25 AU in its radial extent from $p = 1/3$ to 3 bar. At low pressure, the habitability is low and varies with a; at high pressure, the habitability is high and relatively constant inside the HZ. We interpret these results in terms of the pressure dependence of the greenhouse effect, the efficiency of horizontal heat transport, and the extent of the liquid water temperature range. Within the limits discussed in the paper, the results can be extended to planets in eccentric orbits around non-solar-type stars. The main characteristics of the pressure-dependent HZ are modestly affected by variations of planetary properties, particularly at high pressure.

Key words: astrobiology – planetary systems

Online-only material: color figures

1. INTRODUCTION

Observational searches for extrasolar planets are motivated, in large part, by the quest for astronomical environments with physical and chemical conditions supportive of life. The criterion most commonly adopted to define such "habitable" environments is the presence of water in liquid phase. This criterion is motivated by the fundamental role played by water in terrestrial life and by the unique properties of the water molecule (Bartik et al. 2011). Among all types of astronomical environments, only planets and moons may possess the right combination of temperature and pressure compatible with water in the liquid phase. The exact range of planetary physical conditions is determined by a number of stellar, orbital, and planetary factors. The combination of stellar flux and orbital parameters that yield surface planet temperatures compatible with the liquid water criterion defines the circumstellar "habitable zone" (HZ; Dole 1964; Hart 1979; Kasting et al. 1993). The location of the inner and outer boundaries of the HZ depends on many planetary factors and, in particular, on the atmospheric properties that govern the greenhouse effect. The outer limit of the "classic" HZ is calculated allowing for the presence of a geochemical cycle of CO_2 that creates a stabilizing climate feedback; the inner limit takes into account the possibility of a runaway greenhouse effect driven by water vapor (Walker et al. 1981; Kasting et al. 1993; Kasting & Catling 2003; Selsis et al. 2007). Planets with high-pressure, H_2–He atmospheres would be habitable well outside the outer edge of the classic HZ (Pierrehumbert & Gaidos 2011). In the context of HZ studies, the possible existence of habitable exomoons is also under investigation (Reynolds et al. 1987; Williams et al. 1997; Scharf 2006; Heller & Barnes 2013).

The HZ concept was introduced in scientific literature before the first discovery of an extrasolar planet with the radial-velocity method (Mayor & Queloz 1995). The subsequent detection of hundreds of exoplanets with the same method and/or with the transit method has converted the HZ concept into a powerful tool used to discriminate habitable planets on the basis of the orbital semi-major axis, a physical quantity that can be derived from both detection methods. One of the main results of exoplanet observations is the discovery of a great variety of planetary and orbital characteristics not found in the solar system (see, e.g., Udry & Santos 2007; Howard et al. 2012 and references therein). Even if a large region in this parameter space yields conditions not appropriate for liquid water, a fraction of habitable planets are expected to be present. At the present time, the number of planets detected inside or close to the HZ is small (Selsis et al. 2007; Pepe et al. 2011; Borucki et al. 2012; Anglada-Escudé et al. 2012; Tuomi et al. 2013), but this number is expected to increase dramatically in the coming years. In fact, the number of low-mass, terrestrial planets potentially in the HZ is expected to be very high since the planetary initial mass function peaks at low masses (Mordasini et al. 2012) and the multiplicity of planetary systems is higher when low-mass planets are detected (Lo Curto et al. 2010; Lissauer et al. 2011; Latham et al. 2011). Exploratory studies of terrestrial planets in the HZ will set the framework for focusing subsequent, time-consuming investigations aimed at the search for atmospheric biomarkers.

The measurement of the physical quantities relevant for habitability suffers from the limitations inherent to the observational techniques of exoplanets (Udry & Santos 2007). Given the shortage of experimental data on terrestrial-type exoplanets, the study

of their habitability requires a significant effort of modelization. Models of planetary climate are fundamental in this context, since they complement the observational data with quantitative predictions of the physical quantities relevant for assessing their habitability.

A variety of models of planetary climate are currently available, all originated from studies of Earth's climate (McGuffie & Henderson-Sellers 2005). State-of-the-art global circulation models (GCMs) allow us to treat in three dimensions the chemistry and dynamics of the atmosphere, as well as to track the feedback existing between the different components of the climate system. The use of three-dimensional climate models to investigate the habitability of extrasolar planets is quite recent. So far, this technique has been applied to a few planets (or candidate planets) orbiting M dwarf stars (Joshi 2003; Heng & Vogt 2011; Wordsworth et al. 2011). Modeling the climate requires a large number of planetary parameters not constrained by observations of exoplanets. Given the very large amount of computing resources required to run a GCM, the exploration of the parameter space relevant to the climate and habitability requires a more flexible tool.

Energy balance models (EBMs) offer an alternative approach to climate modelization. These models employ simplified recipes for the physical quantities relevant to the climate and require a modest amount of CPU time and a relatively low number of input parameters. The predictive power is limited since EBMs do not consider, among other effects, the wavelength dependence of the radiative transfer and the vertical stratification of the atmosphere. In spite of these limitations, EBMs offer the possibility to estimate the surface temperature at different latitudes and seasons, and are ideal for exploratory studies of habitability. Feedback processes, such as the ice-albedo feedback (Spiegel et al. 2008, hereafter SMS08) or the CO_2 weathering cycle (Williams & Kasting 1997, hereafter WK97) can be implemented, although in a schematic form.

Previous applications of EBMs to extrasolar planets have investigated the dependence of the habitability on axis obliquity, continent distribution, CO_2 partial pressure, rotation period, and orbital eccentricity (WK97; Williams & Pollard 2002; SMS08; Spiegel et al. 2009; Dressing et al. 2010). Climate EBMs have also been used to explore the habitability in the presence of Milankovitch-type cycles (Spiegel et al. 2010), in tidally locked exoplanets (Kite et al. 2011), and around binary stellar systems (Forgan 2012). Predictions of planet IR light curves can also be obtained with EBMs (Gaidos & Williams 2004). Here we introduce a more complete formulation of a planetary EBM, aimed at addressing open conceptual questions in planetary habitability and paleo-climate dynamics. As a first application of this model, in this paper we investigate the influence of atmospheric pressure on planet temperature and habitability. The focus is on the physical effects induced by variations of the total surface pressure, p, at a constant chemical composition of the atmosphere. Surface pressure is a key thermodynamical quantity required to estimate the habitability via the liquid water criterion. At the same time, pressure influences the climate in different ways and the high computational efficiency of EBMs allows us to explore pressure effects under a variety of initial conditions. Here we have made an intensive use of EBM to generate maps of planetary habitability as a function of p and semi-major axis, i.e., a sort of pressure-dependent HZ. The calculations have been repeated for several combinations of orbital and planetary parameters. In particular, we have explored how the climate and habitability are affected by changes of

physical quantities that are not measurable with present-day exoplanet observations.

This paper is organized as follows. The climate model is presented in the next section. Technical details on the model prescriptions and calibration are given in the Appendix. In Section 3 we present the habitability maps obtained from our simulations. The results are discussed in Section 4 and the work is summarized in Section 5.

2. THE CLIMATE MODEL

The simplest way of modeling the climate of a planet is in terms of the energy balance between the incoming and outgoing radiation. The incoming radiation, S, is of stellar origin and peaks in the visible, with variable contributions in the UV and near-IR range, depending on the spectral type of the central star. The outgoing radiation emitted by the planet, I, generally peaks at longer wavelengths and is called the outgoing long-wavelength radiation (OLR). For the planets that can host life, characterized by a surface temperature $T \approx 3 \times 10^2$ K, the OLR peaks in the thermal infrared. In addition, the planet reflects back to space a fraction A of the short-wavelength stellar radiation. This fraction, called *albedo*, does not contribute to the heating of the planet surface. At the zero-order approximation we require that the fraction of stellar radiation absorbed by the planet, $S(1 - A)$, is balanced, in the long term, by the outgoing infrared radiation, i.e., $I = S(1 - A)$.

The zero-order energy balance neglects the horizontal transport, i.e., the exchanges of heat along the planet surface. EBMs provide a simple way to include the horizontal transport in the treatment of planetary climate. In EBMs, the planet surface is divided in strips delimited by latitude circles, called "zones," and the physical quantities of interest are averaged in each zone over one rotation period. The longitudinal heat transport does not need to be explicitly considered since it is averaged in each zone. The treatment of the horizontal transport is thus restricted to that of the latitudinal transport.

Zonally averaged EBMs are one dimensional in the sense that the spatial dependence of the physical quantities only takes into account the latitude, φ, usually mapped as $x = \sin\varphi$. However, with the inclusion of a term describing the effective thermal capacity of the planet surface, one can also introduce the dependence on time, t. At each given time and latitude zone, the thermal state of the atmosphere and ocean is represented by a single temperature, $T = T(t, x)$, representative of the surface temperature. This is the type of model that we consider here. In particular, following previous work on Earth and exoplanet climate (North & Coakley 1979; North et al. 1983; WK97; SMS08), we adopt the *diffusion equation* of energy balance:

$$C\frac{\partial T}{\partial t} - \frac{\partial}{\partial x}\left[D\left(1 - x^2\right)\frac{\partial T}{\partial x}\right] + I = S\left(1 - A\right). \quad (1)$$

In this equation, the efficiency of the latitudinal heat transport is governed by the diffusion coefficient, D, while the thermal inertia of the different components of the climate system is determined by the effective heat capacity, C. The incoming short-wavelength radiation, S, is an external forcing driven by astronomical parameters, such as the stellar luminosity, the orbital semi-major axis and eccentricity, and the obliquity of the planet axis of rotation. The outgoing infrared radiation, I, is largely governed by the physical and chemical properties of the atmosphere. The albedo A is specified by the surface distribution of continents, oceans, ice, and clouds. The physical quantities
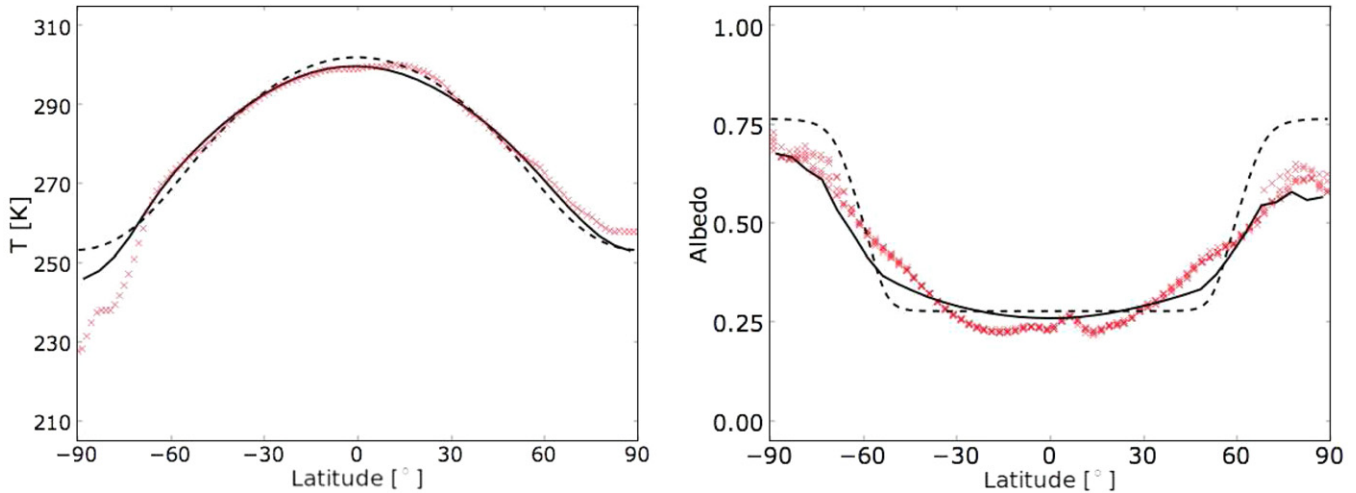
Figure 1. Comparison of experimental data and model predictions of the Earth latitude profiles of mean annual temperature (left panel) and mean annual albedo (right panel). Crosses: average ERA Interim temperatures in the period 1979–2010 (left panel); ERBE short-wavelength albedo in the years 1985–1989 (Pierrehumbert 2010). Solid line: our model. Dashed line: model by SMS08.

(A color version of this figure is available in the online journal.)

generally evolve with time, t. The temporal dependence of EBMs can be used to study seasonal and/or long-term climate effects. In this work we only consider the seasonal evolution. At variance with the zero-dimensional model, the physical quantities in the EBM are zonal, i.e., they depend on $x = \sin \varphi$. The dependence of the physical quantities on t and x may be indirect, via their dependence on the temperature $T = T(t, x)$. Some quantities, such as the albedo of the oceans, depend on the stellar zenith distance, $Z_\star = Z_\star(t, x)$. In spite of its simplicity, the model is able to capture some of the feedback between the main components of the climate system, such as the ice-albedo feedback.

2.1. Physical Ingredients

The degree of realism of the EBM is largely determined by the formalism adopted to describe the physical quantities C, D, I, S, and A. The recipes that we adopt are inspired by previous EBM work published by SMS08, WK97, and North et al. (1983). In our EBM, we have introduced several new features aimed at addressing some limitations of the method and broadening the range of application of the model.

An intrinsic limitation of diffusive EBMs is that the physics that drives the horizontal transport is more complex than implied by the diffusion term that appears in Equation (1). We have introduced a dependence of the diffusion coefficient D on the stellar zenith distance. In this way, the efficiency of horizontal heat transport becomes a function of latitude and orbital phase, as in the case of real planets. In a real planetary atmosphere, heat transport across latitudes is governed by large-scale fluid motions and their instabilities (such as baroclinic instability). Here, such effects are parameterized in an overly simplified way by assuming diffusive transport, albeit with a variable diffusion coefficient.

Previous EBM work has been applied to planets with Earth atmospheric pressure. Given the impact of atmospheric pressure on the climate and habitability, we have generalized the model for applications to terrestrial planets with different levels of surface pressure. With this aim, in addition to the pressure dependence of the diffusion coefficient, D, already considered by WK97, we have also taken into account the pressure

dependence of the OLR, I, and of the effective thermal capacity, C. Our model allows permanent ice covers to be formed and calculates the cloud coverage according to the type of underlying surface. All the above features are presented in the Appendix, where we provide a full description of the method.

2.2. Solving the Diffusion Equation

The diffusion equation (1) is a partial differential equation in two variables, x and t, that can be solved by separating the terms containing the temporal and spatial derivatives. The temporal part can be written in the form $\partial T / \partial t = f(t, T[x])$, which can be solved with the Runge–Kutta method. In practice, we use the routine *odeint* (Press et al. 1992) characterized by an adaptive step size control. To solve the spatial part, $f(t, T[x])$, we use the Euler method. To this end, we discretize x in N equispaced cells, delimited by $(N + 1)$ cell borders, and use a *staggered grid*, i.e., the quantities of interest are calculated at the center of the cells, whereas their derivatives are calculated at the borders. Boundary values are obtained assuming that the diffusion term and the partial derivative of T are null at the poles.

To validate the code, we used the same set of prescriptions of the physical quantities adopted by SMS08 and we verified the capability of the code to reproduce the results published in that paper. As an example, we show in Figure 1 the mean annual temperature–latitude profile of the Earth obtained in this way (dotted line), which is the same as shown in Figure 2 of SMS08 (solid line). We also verified that our code recovers the exactly same seasonal evolution of the zonal temperatures (Figure 3 in SMS08), as well as the "snowball" transition predicted to occur when the latitudinal diffusion is decreased by a factor of nine (Figure 4 in SMS08).

2.3. Model Calibration

After the adoption of our own set of physical recipes, described in the Appendix, the model was calibrated to reproduce the Earth climate data. The calibration was performed by adopting astronomical and planetary parameters appropriate for Earth and tuning the remaining parameters in such a way so as to reproduce the surface temperature and albedo of Earth (Figures 1 and 2).
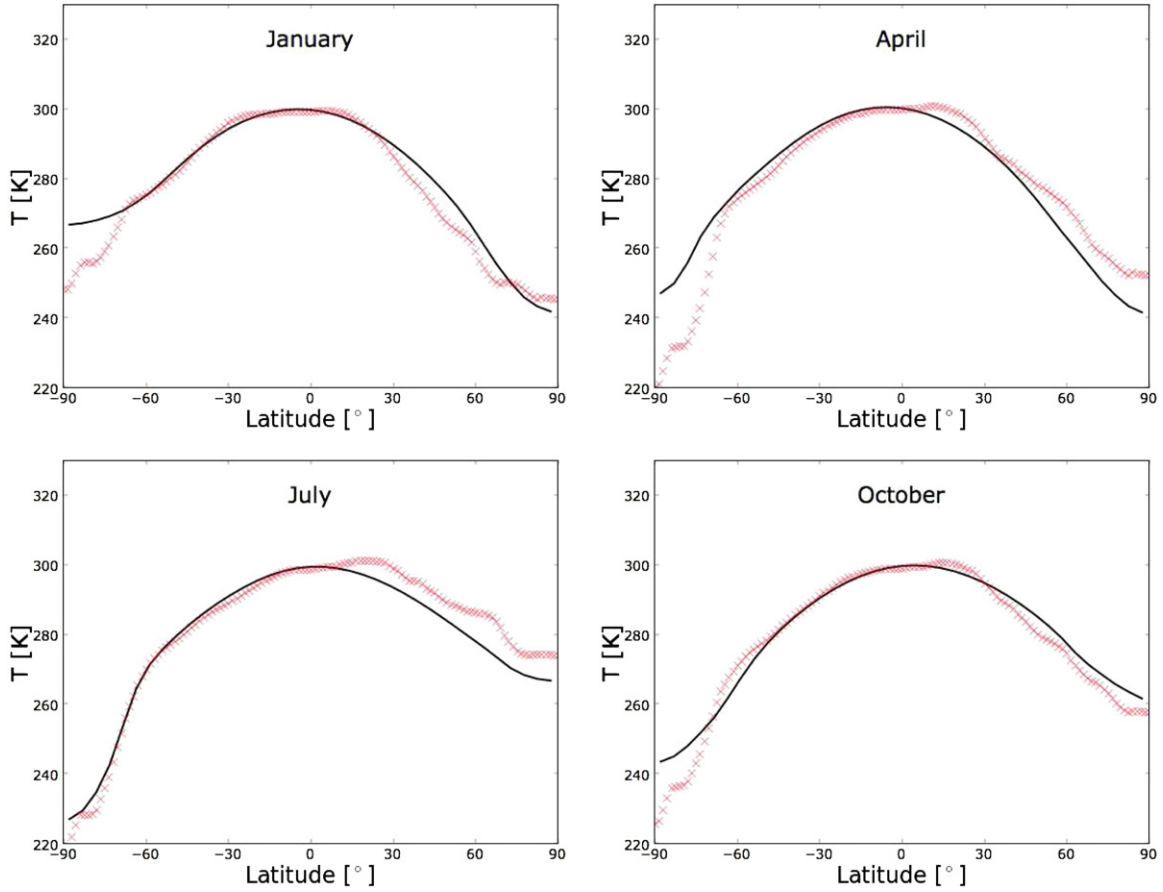
Figure 2. Comparison of experimental data and model predictions of the Earth latitude profiles of mean monthly temperature for January, April, July, and October. Crosses: average ERA Interim data for the same months collected in the period 1979–2010. Solid line: predictions of our EBM.

(A color version of this figure is available in the online journal.)

Table 1
Earth Data

Parameter	Value	Comment
q_0	1361.6 W m^{-2}	Solar constant[a]
a	1.000 AU	Semi-major axis
e	0.01671022	Orbital eccentricity
ϵ	23.43929	Obliquity
$A_{m,\circ}$	0.328	Mean annual global albedo[b]
$T_{m,\circ}$	287.44 K	Mean annual global surface temperature[c]
$p_{t,\circ}$	1.0132×10^5 Pa	Total Earth surface pressure
CO_2	380 ppmV	Volumetric mixing ratio of CO_2
CH_4	1.7 ppmV	Volumetric mixing ratio of CH_4
$c_{p,\circ}$	1.005×10^3 J kg^{-1} K^{-1}	Specific heat capacity of the atmosphere
$m_\circ$	28.97	Mean molecular weight of the atmosphere

Notes.
[a] From Kopp & Lean (2011). The measurement given in that paper, 1360.8 ± 0.5 W m^{-2}, was obtained during the 2008 solar minimum. The excursion between solar minimum and maximum quoted in the same paper amounts to 1.6 W m^{-2}. We have added half this excursion to the value measured at the minimum.
[b] Area-weighted mean annual albedo of Earth measured from the average ERBE data for the period 1985–1989 (data taken from courseware of Pierrehumbert 2010).
[c] Area-weighted mean annual surface temperature of Earth measured from ERA Interim data for the years 1979–2010 (see Dee et al. 2011).

The set of Earth data adopted for the calibration is listed in Table 1. The incoming stellar radiation, $S = S(t, x)$, is fully specified by the solar constant and the Earth orbital parameters and obliquity. The zonal values of Earth ocean fraction f_o, not shown in the table, were taken from Table III of WK97.

The set of fiducial parameters that we adopt for our EBM is shown in Table 2. Some of these parameters are taken from previous work, cited in the last column of the table. Further information on the choice of the parameters is given in the Appendix.

Table 2
Fiducial Model Parameters

Parameter	Fiducial Value	Comment	Equation	Source
$C_{atm,\circ}$	10.1×10^6 J m^{-2} K^{-1}	Effective thermal capacity of the Earth atmosphere	(A1)	Pierrehumbert (2010)
C_{ml50}	210×10^6 J m^{-2} K^{-1}	Effective thermal capacity of the oceans	(A2)	WK97
C_{solid}	1×10^6 J m^{-2} K^{-1}	Effective thermal capacity of the solid surface	(A2)	This work
$D_\circ$	0.600 W m^{-2} K^{-1}	Diffusion coefficient	(A5)	Pierrehumbert (2010)
$\mathcal{R}$	6	Maximum excursion of diffusion efficiency	(A9)	This work
a_l	0.20	Surface albedo of lands	(A13)	WK97
a_{il}	0.85	Surface albedo of ice on lands	(A13)	Pierrehumbert (2010)
a_{io}	0.62	Surface albedo of ice on ocean	(A13)	This work
f_{cw}	0.67	Cloud coverage on water	(A13)	This work
f_{cl}	0.50	Cloud coverage on land	(A13)	This work
f_{ci}	0.50	Cloud coverage on ice	(A13)	This work

After the calibration procedure, our Earth model yields a mean annual global temperature $T_{m,\circ} = 287.8$ K and a mean annual global albedo $A_{m,\circ} = 0.320$, in fine agreement with the Earth values (Table 1). In the left panel of Figure 1, we compare the mean annual temperature–latitude profile predicted by our model (solid line) with experimental data (crosses). The agreement with the observations is excellent in most latitudes, with an area-weighted rms deviation of 2.2 K. However, the model fails to reproduce adequately the temperature profile at Antarctic latitudes. This is likely due to the peculiarities of Antarctica, such as its high elevation with respect to the sea level, that are not accounted for in EBMs. In any case, compared with previous EBM work, our model yields a better agreement at Antarctic latitudes. The predictions of the model of SMS08 are shown for comparison in Figure 1 (dashed line); the model by WK97 predicts a mean annual temperature of 260 K at the southernmost latitudes (see their Figure 4), well above the experimental data.

In the right panel of Figure 1, we compare the mean annual albedo–latitude profile of the Earth predicted by our EBM (solid line) with the experimental data obtained by ERBE for the period 1985–1989 (crosses). The agreement is reasonable but not perfect. The main reasons for disagreement are (1) the over-simplified physical prescriptions of the EBM, which do not consider the atmospheric scattering of the short-wavelength radiation, and (2) the limited amount of fine-tuning of the albedo parameters (e.g., a constant value of albedo for all land). For the sake of comparison, in the same figure we show the mean annual albedo profile obtained with the Earth model of SMS08 (dashed line), where the albedo is a simple function of temperature. At variance with this previous formulation, our parameters can be varied to model the albedo of planets with different types of surfaces. It is worth mentioning that the top-of-atmosphere recipes for the albedo given by WK97, which include a treatment of atmospheric scattering, cannot be applied to the present work. This is because the radiative–convective calculations of WK97 were performed by varying the concentration of CO_2, while we are interested in varying the total pressure keeping the composition fixed.

Careful inspection of the seasonal dynamics shows that in the northern hemisphere the temporal evolution of the model slightly lags that of the data (see Figure 2). This is probably due to an intrinsic limitation of one-dimensional EBMs, related to the calculation of the zonal thermal capacity: the zonal average of C tends to be overestimated in zones with ocean fractions above ≈ 0.1 because the effective thermal capacity of the oceans is much higher than that of the lands (WK97). As a consequence, our EBM overestimates the thermal inertia at the mid-northern

latitudes of Earth (with ocean fractions $f_o = 0.3$–0.5) and predicts that the seasonal temperature should vary more slowly than is observed.

For the purpose of this investigation, an important feature of the temperature profile is the location of the ice line, which affects the calculation of planetary habitability. To test this feature, we compared the latitude $\varphi_\circ$ where $T = 273$ K in our EBM and in the Earth data. We find a mean annual difference $\langle \varphi_{\circ,model} - \varphi_{\circ,data} \rangle = +0°.6 \pm 3°.2$ in the southern hemisphere and $-2°.4 \pm 10°.4$ in the northern hemisphere (average over 12 months). The small offset $\langle \varphi_{\circ,model} - \varphi_{\circ,data} \rangle$ in both hemispheres testifies in favor of the quality of the ice line calibration. The large scatter in the northern hemisphere is due to the above-discussed seasonal time lag resulting from the overestimate of the thermal capacity.

More details on the model calibration are given in the Appendix, where we show that, in addition to the temperature and albedo data, also the OLR data of Earth have been used to constrain our EBM (see Appendix A.3).

3. APPLICATIONS TO EXOPLANETS

The climate model presented in the previous section is a flexible tool that allows us to explore part of the huge parameter space relevant for the study of planetary habitability. The physical quantities that enter into the EBM are quite numerous and it is important to make a distinction between those that are observable and those that are not in the case of exoplanets. In the present work, we generate maps of habitability in a two-dimensional space built up in such a way so as to explore how a parameter unconstrained by observations influences the habitability while we vary an observable physical quantity. In this way, we investigate the effects of unconstrained parameters against an experimental parameter space where one can place observed exoplanets.

The choice of the observational quantities that we use in our maps is dictated by their relevance to the climate. Luckily, at least some of the model parameters most relevant to the planet's climate can be constrained by observations. This is true for the stellar flux, the semi-major axis, and the eccentricity of the planet orbit. These three parameters can be combined to derive the mean annual level of insolation, a fundamental parameter for the climate. To define the HZ in our maps, we will show the correspondence between this quantity and the semi-major axis for the case of planets orbiting a solar-like star.

Among the quantities unconstrained by observations, the axis obliquity and CO_2 partial pressure have been investigated in previous work (WK97; Spiegel et al. 2009). Here we focus on

the surface pressure, p, in planets with Earth-like atmospheres. Our maps of habitability therefore have the semi-major axis or insolation in the abscissae and the surface pressure in the ordinates. In this section, we explain how we generate this type of map. In the next section we investigate how the results that we obtain are influenced by other unconstrained planetary parameters, such as axis obliquity, rotation period, geography, and albedo.

3.1. Running the Simulations

To investigate the effects of surface pressure on the location of the HZ, we generate a large number of models of an Earth-like planet by varying a and p while keeping constant the other orbital and planetary parameters. To focus our problem, we consider an atmosphere with an Earth-like composition but variable level of total pressure. In practice, we scale the partial pressures of non-condensable gases by a constant factor. In this way, the mixing ratios of non-condensable greenhouses, such as CO_2 or CH_4, are always equal to that of the Earth atmosphere. The mixing ratio of water vapor is instead set by the temperature and relative humidity. This scaling of the pressure is in line with the assumptions adopted in the calibration of the OLR described in Appendix A.3.

Each simulation starts with an assigned value of temperature in each zone, T_{start}, and is stopped when the mean global annual temperature, T_m, converges within a prefixed accuracy. In practice, we calculate the increment δT_m every 10 orbits and stop the simulation when $|\delta T_m| < 0.01$ K. The convergence is generally achieved in fewer than 100 orbits. Tests performed with widely different values of $T_{start} > 273$ K indicate that the simulations converge to the same solution. We adopted a value of $T_{start} = 275$ K, just above the threshold for ice formation, so that the simulation starts without ice coverage and without artificial triggering of snowball episodes. The choice of a low value of T_{start} is dictated by our interest in exploring a wide range of pressures: $T_{start} = 275$ K is below the water boiling point even at very low values of pressure, when the boiling point is just a few kelvin above the freezing point.

The starting value of total pressure p in the simulations is the total pressure of non-condensable gases, i.e., the "dry air" pressure. In the course of the simulation, p is updated by adding the current value of the partial pressure of water vapor. This is calculated as

$$p\mathrm{H_2O} = rh \times p_{sat,w}(T), \qquad (2)$$

where rh is the relative humidity and $p_{sat,w}(T)$ is the saturated water vapor pressure.[4] Also the specific heat capacity, c_p, and the mean molecular weight, m, of the atmosphere are recalculated at each orbit taking into account the contribution of water vapor. The thermal capacity and the diffusion coefficient, which depend on c_p and m, are also updated.

In addition to the regular exit based on the convergence criterion, the simulations are stopped when the mean planet temperature exceeds some prefixed limits (T_{min}, T_{max}). This forced exit without convergence is introduced to minimize the computing time when we run a large number of simulations, as in our case. We adopt $T_{min} = 220$ K, well below the limit of liquid water habitability. The value of T_{max} is based on the water-loss limit criterion explained below. When T_m is outside the

interval (T_{min}, T_{max}), the simulation is stopped and the indices of habitability are set to zero.

The existence of a planetary water-loss limit is based on the following arguments. At a given value of relative humidity, $p\mathrm{H_2O}$ increases with temperature according to Equation (2) because the saturated pressure of water vapor increases with T. The dominant feedback mechanism of water vapor is the enhancement of the IR opacity, which tends to raise the temperature. In extreme cases, this positive feedback may lead to a complete water vaporization via a runaway greenhouse effect, followed by a loss of hydrogen in the upper atmosphere via EUV stellar radiation. All together, these effects indicate the existence of a temperature limit above which water is lost from the planet. In the case of Earth, the water-loss limit is predicted to occur at $\simeq 340$ K, while for a planet with $p = 5$ bar at $\simeq 373$ K (Selsis et al. 2007 and references therein). These values of temperature approximately lie at 90% of the liquid water temperature range calculated at the corresponding value of pressure. On the basis of these arguments, we adopt as a water-loss limit the value

$$T_{max} = T_{ice}(p) + 0.9 \times [T_{vapor}(p) - T_{ice}(p)], \qquad (3)$$

where $T_{ice}(p)$ and $T_{vapor}(p)$ are the melting and boiling points of water at pressure p (Lide 1997). The adoption of the water-loss limit (3) minimizes the difficulty of tracking the effects of water vapor in the atmosphere when the temperature is high (see Appendix A.3). The results on runaway water-loss events are conservative given our choice of adopting a "cold start" in the simulations.

3.2. Indices of Mean Temperature and Habitability

For each set of input parameters, our simulations provide a matrix of surface temperatures calculated at discrete values of latitude and time, $T(\varphi, t)$. We use different tools to analyze these results. To cast light on specific cases, we investigate the latitude–temperature profile and its seasonal evolution. To have a global view of a large set of results, we build up maps of mean annual global temperature and habitability.

We call *mean planet temperature*, T_m, the mean global annual temperature at the planet surface. To calculate this quantity, we average $T(\varphi, t)$ on latitude and time. The average on latitude is weighted in area.

To estimate the surface habitability from the results of our simulations, we require that the temperature and the pressure lie within the range of liquid water in the phase diagram of H_2O. We consider values of total pressure above the triple point and below the critical pressure. Within this interval, we define a *habitability function* such that

$$H(\varphi, t) = \begin{cases} 1 & \text{if } T_{ice}(p) \leqslant T(\varphi, t) \leqslant T_{vapor}(p) \\ 0 & \text{otherwise.} \end{cases} \qquad (4)$$

Several indices of surface habitability can be defined by integrating $H(\varphi, t)$ in different ways. Following SMS08, we introduce the temporal habitability

$$f_{time}(\varphi) = \frac{\int_0^P dt\, H(\varphi, t)}{P}, \qquad (5)$$

i.e., the fraction of orbital period P in which the planet is habitable at a given latitude, and the regional habitability

$$f_{area}(t) = \frac{\int_{-\pi/2}^{+\pi/2} d\varphi\, [H(\varphi, t)\cos\varphi]}{2}, \qquad (6)$$

---

[4] We adopt $p_{sat,w}(T) = e^{(77.3450+0.0057\,T-7235/T)}/T^{8.2}$, a relation that yields an excellent agreement with the values tabulated in the CRC Handbook of Chemistry and Physics (Lide 1997). See also http://www.engineeringtoolbox.com/water-vapor-saturation-pressure-air-d_689.html.
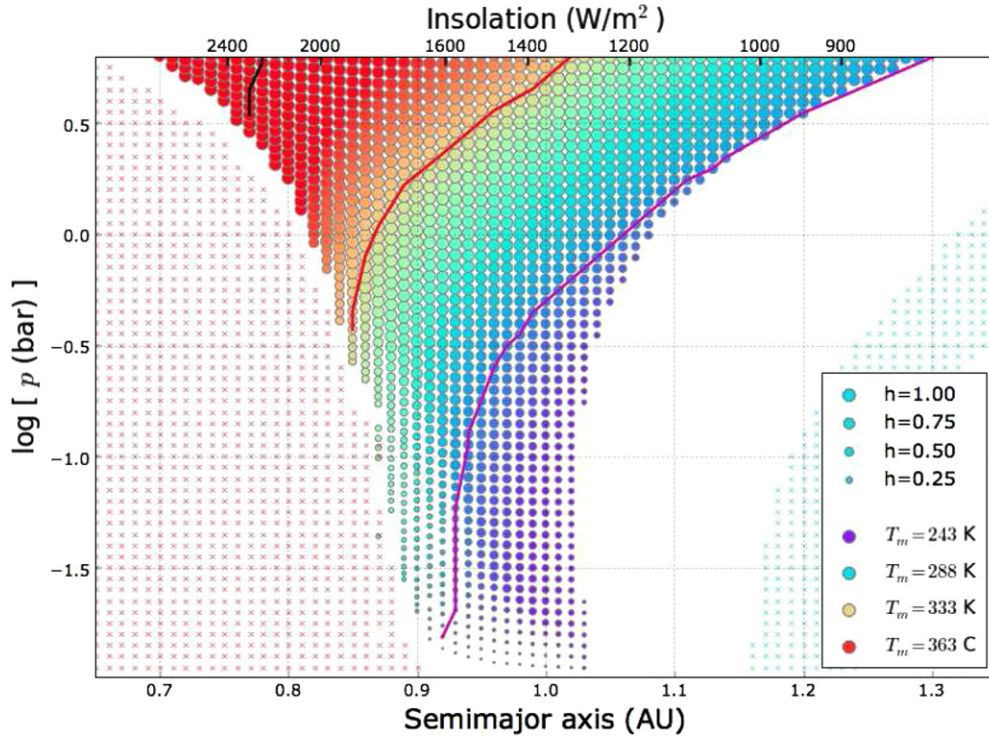
Figure 3. Circumstellar HZ of planets with Earth-like atmospheres and different levels of surface pressure obtained with our EBM climate simulations. Abscissae: semi-major axis, a (bottom axis), or insolation $q = L_\star/(4\pi a^2)$ (top axis). Ordinates: logarithm of the total surface pressure, p. The circles indicate solutions with mean global annual habitability $h > 0$. The area of the circles is proportional to h; the colors are coded according to the mean annual global surface temperature, T_m. The size and color scales are shown in the legend. The solid lines are contours of equal mean temperature $T_m = 273$ K (magenta), 333 K (red), and 393 K (black). Results above the contour at $T_m = 333$ K (red line) are tentative; see Section 3.3. Red crosses: simulations stopped on the basis of the water-loss limit criterion (Equation (3)); blue crosses: simulations interrupted when $T_m < T_{\min}$; see Section 3.1. Adopted model parameters are listed in Tables 2 and 3.
(A color version of this figure is available in the online journal.)

i.e., the fraction of planet surface that is habitable at a given time. By integrating the habitability function both in latitude and time, we obtain the mean global annual habitability

$$h = \frac{\int_{-\pi/2}^{+\pi/2} d\varphi \int_0^P dt \, [H(\varphi, t) \cos\varphi]}{2P}. \qquad (7)$$

This represents the *mean fraction of planet surface that is habitable during the orbital period*.

In addition to these indices, already defined by SMS08, we introduce here the index of continuous habitability

$$h_c = \frac{\int_{-\pi/2}^{+\pi/2} d\varphi \, f'(\varphi) \cos\varphi}{2}, \qquad (8)$$

with

$$f'(\varphi) = \begin{cases} 1 & \text{if } f_{\text{time}}(\varphi) = 1 \\ 0 & \text{if } f_{\text{time}}(\varphi) < 1. \end{cases} \qquad (9)$$

The index h_c represents the *fraction of planet surface that is continuously habitable during the orbital period*. This index vanishes if all the latitude zones undergo a period of non-habitability in the course of the orbital period. By construction, it is always $h_c \leqslant h$.

3.3. Habitability Maps

In Figure 3, we show the map of habitability obtained from our simulations for an Earth-like planet in circular orbit around a Sun-like star. To obtain this figure, we run a total of 4032 simulations covering the interval of semi-major axis

Table 3
Model Parameters Fixed in the Simulations

Parameter	Adopted Value	Comment
N	37	Number of latitude zones
$L_\star$	$L_\odot$	Stellar luminosity[a]
$M_\star$	$M_\odot$	Stellar mass[b]
e	0.00	Orbital eccentricity
ω	0.00	Argument of the pericenter
ϵ	23.44	Axis obliquity
g	9.8 m s^{-2}	Surface gravitational acceleration[c]
P_{rot}	1 day	Rotation period
f_o	0.70	Ocean fraction (constant in all latitude zones)

Notes.
[a] The solar luminosity $L_\odot$ is calculated from the adopted value of solar constant, q_0 (Table 1).
[b] The stellar mass, in conjunction with the semi-major axis a, determines the orbital period adopted in each simulation.
[c] The surface gravitational acceleration is used in the radiative calculations of the OLR (Appendix A.3).

$0.65\,\text{AU} \leqslant a \leqslant 1.35\,\text{AU}$, with a step $\delta a = 0.01$ AU, and the interval of pressure $10^{-2.0}\,\text{bar} \leqslant p \leqslant 10^{+0.8}\,\text{bar}$, with a constant logarithmic step $\delta \log p\,(\text{bar}) = 0.05$. The values of the parameters that are kept constant in these simulations are listed in Table 3.

The map of Figure 3 shows the results obtained at each point of the plane (a, p) in terms of mean annual global temperature and habitability. The filled circles in the map indicate the positions in the plane (a, p) where $h > 0$; the

value of total pressure associated to these symbols includes the partial pressure of water vapor updated in the course of the simulation. Crosses indicate positions on the plane where the simulations were forced to exit; the total pressure for these cases is the starting value of dry air pressure (see Section 3.1). Empty areas of the map, as well as crosses, indicate a location of non-habitability.

The simulations yield information not only on the degree of habitability, through the index h, but also on the "quality" of the habitability, through a detailed analysis of the seasonal and latitudinal variations of the temperature, as we shall see in the next section. However, some cautionary remarks must be made before interpreting these data.

The model has been calibrated using Earth climatological data. These data span a range of temperatures, roughly 220 K $\lesssim T \lesssim$ 310 K, not sufficient to cover the broad diversity expected for exoplanets, even if we just consider those of terrestrial type. Given the fundamental role of temperature in the diffusion equation, one should be careful in using the physical quantities outside this range, where direct calibration is not possible. In this respect, the major reason of concern is the estimate of the OLR that has been done with radiative calculations (see Appendix A.3). The difficulty of calibrating the OLR outside the range of terrestrial temperatures makes uncertain the exact localization of the inner and outer edges of the HZ. In particular, the results with $T_m \gtrsim$ 330 K should be treated with caution, given the strong effects of water vapor predicted to occur in this temperature range, which are not directly testable. These cases lie in the region of high pressure in Figure 3 (symbols color-coded in orange and red). The fact that in these cases also the pressure is quite different from the Earth value makes these results particularly uncertain. In the following discussion, we will consider these particular results to be purely tentative. We note that the difficulty of making climate predictions outside the parameter space sampled by the Earth is a common problem of any type of climate model, no matter how sophisticated. In this respect, simple models, like our EBM, help to obtain preliminary predictions to be tested by subsequent investigations.

4. DISCUSSION

In this section, we describe and interpret the complex patterns that we find in the pressure-dependent map of planet temperature and habitability of Figure 3. We then discuss how the results can be extended to more general situations other than circular orbits of planets orbiting a Sun-like star. We conclude this section setting our results in the context of previous studies.

4.1. The Pressure-dependent Habitable Zone

The circumstellar HZ shown in Figure 3 shows several characteristics, in terms of mean planet temperature and habitability, that can be summarized as follows.

The radial extent of the HZ increases with p. The outer edge extends from 1.02 to 1.18 AU when the pressure rises from 0.1 to 3 bar. The inner edge approaches the star from 0.87 to 0.77 AU in the same pressure interval. No habitability is found below $p \simeq$ 15 mbar.

The broadening of the HZ with increasing pressure is accompanied by an increase of the interval of mean planet temperatures spanned at constant p. At high pressures, most of the broadening of the HZ is contributed by the area of the plane where the solutions have mean temperatures $T_m \gtrsim 60°$C (i.e., $T_m \gtrsim$ 333 K;

orange and red symbols above the red line in the figure). If we focus on the interval of mean temperatures $0°$C $\lesssim T_m \lesssim 60°$C (region with 273 K $\lesssim T_m \lesssim$ 333 K between the magenta and red line), the broadening of the HZ is quite modest.

Remarkable differences exist between the low- and high-pressure regimes. At low pressures ($p \lesssim$ 0.3 bar) the habitability undergoes intense variations in the plane (a, p), with a general trend of increasing h with increasing p. At high pressure ($p \gtrsim$ 1 bar) the habitability is approximately constant and high, with sudden transitions from $h \simeq 1$ inside the HZ, to $h \simeq 0$. The mean planet temperature also shows different characteristics between the low- and high-pressure regimes. Starting from pressure $p \gtrsim$ 0.3 bar, the curves of equal temperature tend to move away from the star as the pressure increases. This behavior is not seen at lower pressures, where the HZ at a given temperature does not significantly change its distance from the star.

Another interesting feature of Figure 3 is the location of the line of constant mean planet temperature $T_m = 273$ K, indicated as a magenta solid line superimposed on the symbols of habitability. On the basis of the liquid water habitability criterion, one would expect a coincidence of this line with the outer edge of the HZ. This is true at $p \gtrsim$ 2 bar, but not at lower values of pressure, the mismatch being quite large at the lowest values of pressure considered. The reason is that, using an EBM, we can determine whether some latitudinal zones have temperatures larger than zero, even when the mean planet temperature is lower. When this is the case, the planet is partly habitable.

Further insight on the differences between low and high pressures is offered by Figure 4, where we plot the surface habitability and temperature as a function of p. The three panels of the figure show the results obtained at three constant values of semi-major axis (i.e., insolation). In addition to the habitability h (lower solid curve) and the mean planet temperature T_m (upper solid curve), we show the minimum and maximum planet temperature dot-dashed and dashed curves, respectively). These temperatures are measured regardless of the time of year or of the latitude, i.e., the maximum temperature could be found at low latitudes and in summer, while the minimum, at high latitudes in winter. The general rise of mean temperature and habitability with increasing pressure is clear in each case. Moreover, one can see that the excursion between extreme temperatures is quite large at low pressure ($\Delta T \sim$ 100–200 K), but becomes increasingly smaller as the pressure rises. Planets with high atmospheric pressure have a rather uniform surface temperature.

The rich phenomenology described above results from the interaction of distinct physical factors that we now discuss.

4.2. Interpretation

The links between surface pressure and habitability are rather intricate. Pressure variations influence both the planet temperature and the extent of the liquid water temperature interval used to define the habitability. To disentangle these effects we first discuss the influence of pressure on the temperature and then on the habitability.

4.2.1. Surface Pressure and Planet Temperature

Variations of surface pressure affect the temperature in two ways. First, for a given atmospheric composition, the infrared optical depth of the atmosphere will increase with pressure. As a result, a rise of p will always lead to a rise of the greenhouse effect and temperature. Second, the horizontal heat transport increases with pressure. In our model, this is reflected by the linear increase with p of the diffusion coefficient D
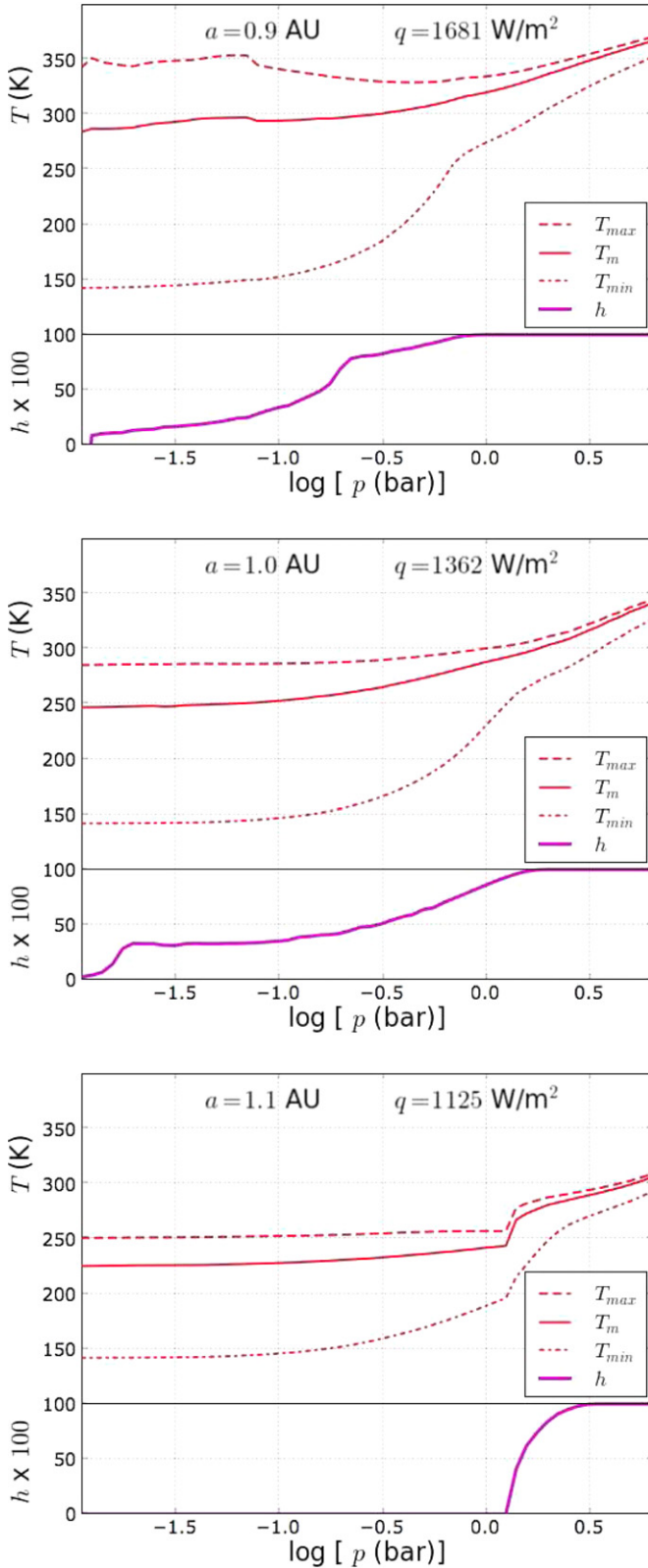
Figure 4. Planet surface temperature, T, and habitability, h, as a function of surface pressure, p. Each panel shows the results obtained at constant semi-major axis, a, and constant insolation, q, indicated in the legend. The solid curve at the bottom of each panel is the habitability expressed in percent units. The three curves at the top of each panel are temperature curves in kelvin units (solid line: mean planet temperature; dot-dashed and dashed lines: minimum and maximum planet temperatures at any latitude and season). Adopted model parameters are listed in Tables 2 and 3.

(A color version of this figure is available in the online journal.)

(Equation (A5), Appendix A.2). At variance with the first effect, it is not straightforward to predict how the temperature will react to a variation of the horizontal transport.

In the case of Earth, our EBM calculations predict a rise of the mean temperature with increasing D. This is due to the fact that the increased diffusion from the equator to the poles tends to reduce the polar ice covers and, as a consequence, to reduce the albedo and raise the temperature. However, our calculations predict the existence of particular types of climates in which a higher diffusion yields a lower mean temperature. An example is shown in the left panel of Figure 5, where we show the mean annual temperature–latitude profile for a planet at $a = 1.0$ AU with $p = 10^{-1.2}$ bar. Most of the planet is frozen, with the exception of an equatorial belt. In these conditions, an increase in the diffusion will decrease the equatorial temperature and extend the ice cover toward low latitudes; in turn, the increase of the ice cover will cool the planet via albedo feedback. Detailed EBM calculations of this type indicate that the initial ice coverage plays a key role in determining the response of T_m to a variation of the latitudinal transport. When the initial ice cover is modest, an increase of D heats the planet, as in the case of Earth. When the initial ice cover is somewhat above $\approx 50\%$, an increase of D might cool the planet, as in the example discussed above; in these cases the cooling may lead to a snowball transition driven by the ice-albedo feedback.

The total effect of pressure variations on temperature will depend on the relative strengths of the greenhouse and latitudinal diffusion effects discussed above. If the greenhouse effect dominates, an increase of p will always raise the temperature at a given a, i.e., at a given insolation $q = L_\star/(4\pi a^2)$. The results that we find in Figure 3 are in line with this expectation when the pressure is sufficiently high, specifically at $p \gtrsim 10^{-0.5}$ bar. However, when the atmospheric column density of greenhouse gases is sufficiently low, pressure variations will not significantly affect the optical depth and temperature. This probably explains the absence of a temperature rise with increasing p in the regime of very low pressures, visible in Figure 4. In this regime, an increase of pressure and diffusion may cool the planet.

As shown in Figure 4, pressure variations not only influence the mean temperature, but also the excursion between minimum and maximum planet temperature. The fact that this excursion becomes increasingly smaller with rising p is due to the increase of diffusion efficiency at high pressures. The high efficiency of the horizontal transport tends to cancel seasonal and latitudinal variations in the surface temperature of the planet. At the other extreme, planets with low atmospheric pressure do not benefit from this heat distribution and undergo large excursions in surface temperature at different latitudes and orbital phases.

For completeness, we mention that pressure variations also affect the thermal inertia of the atmosphere and, as a result, the timescale of adjustment of the planet temperature to seasonal and latitudinal variations of the radiative forcing. In our model, this effect is incorporated in Equation (A1) discussed in Appendix A.1. This effect becomes important only when the fraction of oceans is modest.

4.2.2. Surface Pressure and Planetary Habitability

The location of the inner and outer edges of the HZ is related to the boiling and freezing points of water, respectively. The temperature of the boiling point increases with p, while that of the freezing point is basically constant. As the pressure increases, neglecting any other factor, one would expect the
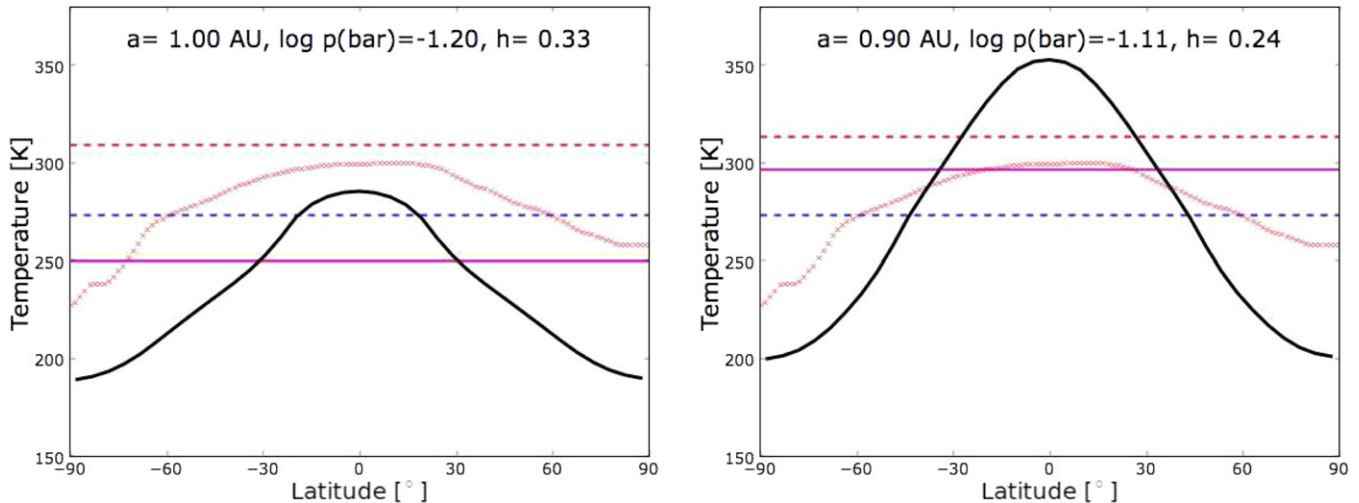
Figure 5. Solid curve: mean annual temperature–latitude profile of an Earth-like planet with semi-major axis, a, surface pressure, p, and habitability, h, specified in the legend of each panel. Solid horizontal line: mean annual global temperature, T_m. Dashed horizontal lines: liquid water temperature interval at pressure p. Adopted model parameters are listed in Tables 2 and 3. Temperature–latitude profiles are symmetric as a result of the idealized geography used in the simulation (constant fraction of oceans in all latitude zones). Crosses: Earth data as in Figure 1.

(A color version of this figure is available in the online journal.)

inner edge of the HZ to approach the star and the outer edge to stay at $a \approx$ constant. The inner edge of the HZ in Figure 3 confirms this expectation. The outer edge, instead, moves away from the star as the pressure increases. This is due to the pressure–temperature effects described above: at high pressure the greenhouse effect becomes more important with increasing p and the planet can remain above the freezing point at increasing a. At the inner edge, the rise of the boiling point dominates over the pressure–temperature effects. For considerations about the kind of life that can be expected at these high temperatures, see Section 4.5.2.

At low pressures the situation is quite complicated. When $p \lesssim 2$ bar, the contour with $T_m = 273$ K (magenta line in the figure) does not overlap with the outer edge of the HZ. In fact, there is an area of the plane (a, p) where planets are habitable even if T_m is below freezing point. This can be understood from the analysis of the latitude–temperature profiles of planets lying in this area of the map. The example at $a = 1.0$ AU with $p = 10^{-1.2}$ bar (left panel of Figure 5) explains this apparent discrepancy. As one can see, even if the mean temperature T_m (solid horizontal line) is below freezing point (lower horizontal dashed line) the existence of a tropical zone of the planet with temperatures above freezing point yields a habitability $h = 0.33$.

Another peculiar feature of Figure 3 is the existence of planets with T_m well inside the liquid water range but with low levels of habitability. An example of this type is shown in the right panel of Figure 5. The mean temperature T_m (solid horizontal line) lies between the freezing and boiling points (horizontal dashed lines), but the habitability is only $h = 0.24$. The temperature–latitude profile explains the reason for this low habitability: most of the planet surface lies outside the liquid-water range because the equatorial belt is above the boiling point and the high latitude zones below the freezing point.

These examples clearly indicate that the mean planet temperature is not a good indicator of habitability when the planet pressure is low.

The pressure dependence of the horizontal heat transport also plays an important role in determining the characteristics of habitability. As discussed above, planets with high pressure have

a uniform surface temperature as a result of the high diffusion. The consequence in terms of habitability is that all the planet surface is either within or outside the liquid water temperature range. If a planet with high pressure lies inside the HZ, its habitability will be $h \simeq 1$. If the temperature goes outside the liquid water range, all the planet surface will become unhabitable. This explains the sudden transitions from $h \simeq 1$ to $h \simeq 0$ that we see in the upper part of Figure 3 when we go out of the HZ.

4.3. Effects of Physical Quantities Constrained by Observations

In addition to the semi-major axis, the orbital eccentricity and the stellar properties can be measured in the framework of observational studies and are relevant for the climate and habitability of exoplanets. The results shown in Figure 3 have been derived for circular orbits and solar-type stars. Here we discuss the extent to which we can generalize these results for eccentric orbits and non-solar-type stars.

4.3.1. Eccentric Orbits

To investigate the dependence of the results on orbital eccentricity we produced a map of habitability in the plane (a, e) for an Earth-like planet with surface pressure $p = 1$ bar. For the ocean fraction we adopted $f_o = 0.7$ constant at all latitudes. All the remaining parameters were kept constant, with the values indicated in Table 3. A total number of 2544 simulations were run to cover the interval of semi-major axis $0.6 \leqslant a \leqslant 1.56$ with a step $\delta a = 0.02$ and the interval of eccentricities $0 \leqslant e \leqslant 0.95$ with a step $\delta e = 0.02$.

In Figure 6, we show the resulting map of habitability and mean planet temperature in the plane (a, e). A characteristic feature of this map is that the distance of the HZ increases with increasing eccentricity. To interpret this effect, we recall that the mean annual flux received by a planet in an elliptical orbit with semi-major axis a and eccentricity e varies according to the law (see, e.g., Williams & Pollard 2002)

$$\langle q \rangle = \frac{L_\star}{4\pi a^2 (1-e^2)^{1/2}}. \tag{10}$$
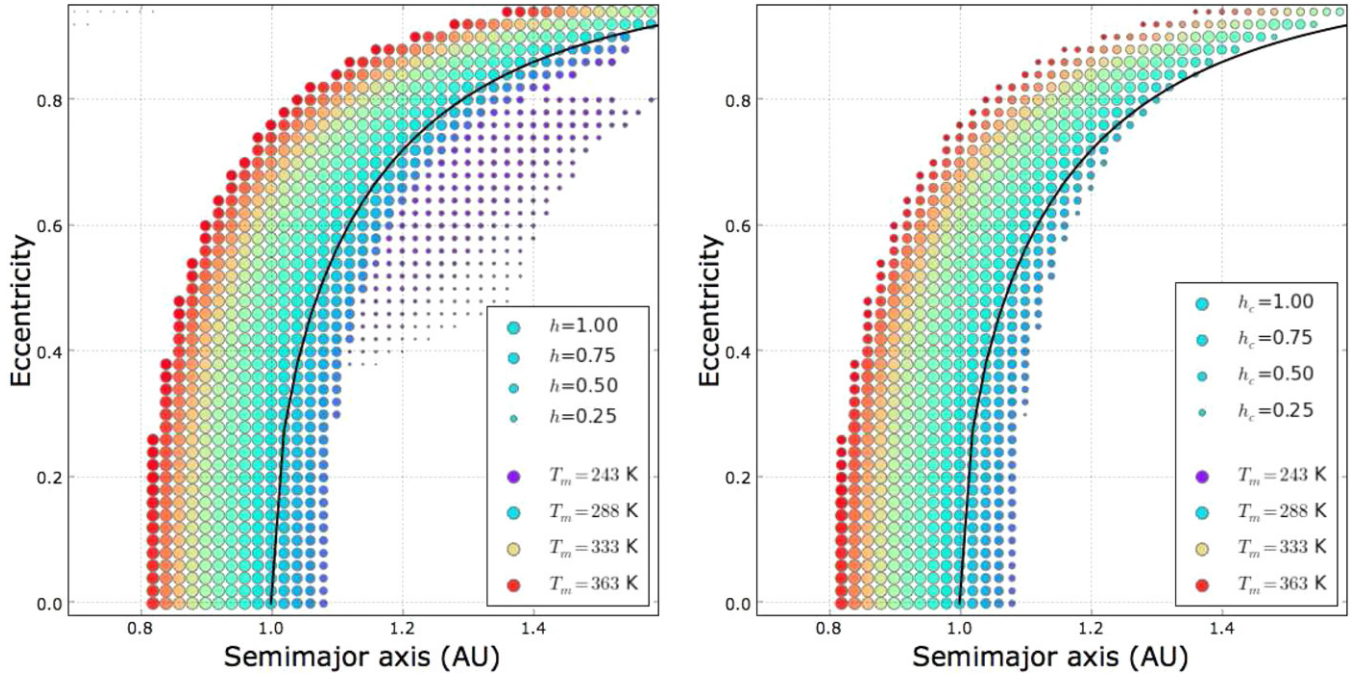
Figure 6. Maps of mean temperature and habitability of an Earth-like planet in the plane of the semi-major axis and eccentricity. Left panel: habitability h; right panel: continuous habitability h_c (see Section 3.2). The area of the circles is proportional to the mean fractional habitability; the color varies according to the mean annual global surface temperature, T_m. The size and color scales are shown in the legend. Adopted model parameters are listed in Tables 2 and 3, with the exception of the eccentricity that has been varied as shown in the figure. Solid curve: line of equal mean annual flux $\langle q \rangle = q_0$ estimated from Equation (10).

(A color version of this figure is available in the online journal.)

Therefore, compared to a circular orbit of radius a and constant insolation $q_0 = L_\star/4\pi a^2$, the mean annual flux in an eccentric orbit increases with e according to the relation $\langle q \rangle = q_0(1 - e^2)^{-1/2}$. In turn, this increase of mean flux is expected to raise the mean temperature T_m. This is indeed what we find in the results of the simulations. The rise of T_m at constant a can be appreciated in the figure, where the symbols are color-coded according to T_m. To test this effect in a quantitative way, we superimpose on the figure the curve of constant mean flux $\langle q \rangle = q_0$, calculated from Equation (10) for $L_\star = L_\odot$. One can see that the HZ follows the same type of functional dependence, $e \propto (1 - a^{-4})^{1/2}$, of the curve calculated at constant flux. This result confirms that the increase of mean annual flux is the main effect that governs the shift of the HZ to larger distances from the star as the eccentricity increases.

A second characteristic feature of Figure 6 is that the habitability tends to decrease with increasing eccentricity. This effect is more evident when we consider the map of continuous habitability, h_c, in the right panel of the figure. The effect is related to the large excursion of the instantaneous stellar flux along orbits that are very elongated. The maximum excursion of the flux grows as $[(1 + e)/(1 - e)]^2$, and therefore exceeds one order of magnitude when $e > 0.5$. As a consequence of this strong flux variation, the fraction of orbital period in which the planet is habitable at a given latitude must become increasingly smaller as the orbit becomes more elongated. This is equivalent to saying that $f_{\rm time}(\varphi)$ decreases and therefore also h and h_c decrease (Section 3.2) with increasing e. The effect on h_c must be stronger because this quantity depends on $f_{\rm time}(\varphi)$ via Equation (9). The comparison between the left and right panels of Figure 6 indicates the existence of an area of the plane (a, e), at high values of a and e, populated by planets that are habitable in small fractions of their orbit. This is demonstrated by the fact that such a population disappears when we consider the continuous habitability h_c. Apart from the existence of this area, it is clear from these figures that the radial extent of the HZ tends to decrease with increasing eccentricity.

On the basis of the above results, it is clear that if the eccentricity is relatively small, the radial extent of the HZ can be scaled according to the mean annual flux. To this end, we introduce the *effective circular semi-major axis*

$$a_{\rm eff} = a(1 - e^2)^{1/4}. \qquad (11)$$

Planets in eccentric orbits have a mean annual flux $\langle q \rangle = L_\star/4\pi a_{\rm eff}^2$. In Figure 7, we plot several curves of habitability calculated at different values of eccentricity using $a_{\rm eff}$ in the abscissa. One can see that, as long as the eccentricity is small ($e \lesssim 0.5$) the curves of habitability versus $a_{\rm eff}$ calculated at different eccentricities show a good overlap. At high eccentricity the curves of habitability do not overlap. The strong effect of eccentricity on the continuous habitability h_c is evident in the right panel of Figure 7. However, even using the index h_c, the curves of habitability versus $a_{\rm eff}$ are almost independent of e when the orbits have low eccentricity.

We conclude that, in studies of planetary habitability, it is possible to use $a_{\rm eff}$ as a proxy of a as long as the eccentricity is sufficiently small. In this way, we can explore the effects on habitability of physical quantities other than a and e while varying a single parameter that conveys the information of the orbital characteristics more relevant to the habitability. However, for highly elongated orbits with $e > 0.5$, one should perform a specific calculation taking into account both a and e.

The influence of orbital eccentricity on planet temperature and habitability has been previously investigated by Williams & Pollard (2002) and Dressing et al. (2010). For comparison with these studies, we calculated the mean global planet temperature as a function of orbital longitude for orbits with $e = 0.1$, 0.3, and 0.4. As a result, we find seasonal trends similar to those
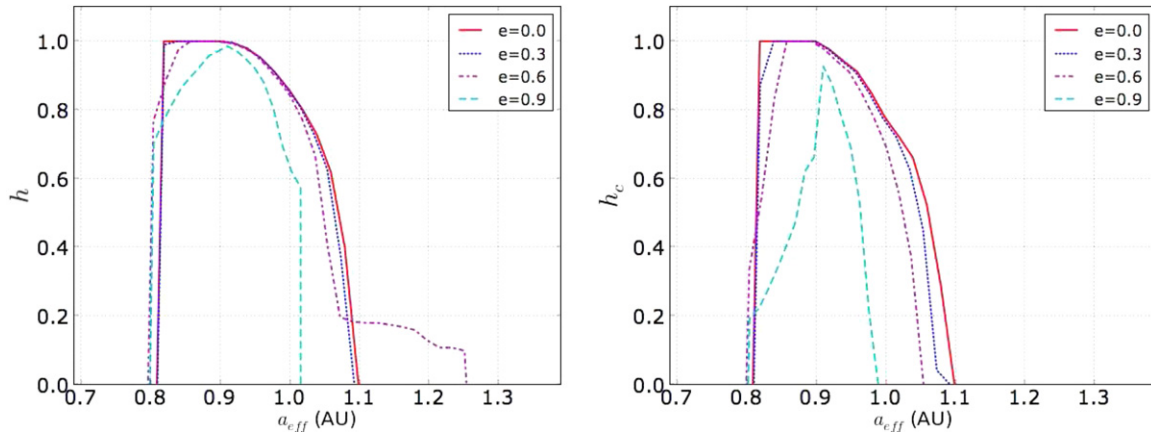
Figure 7. Radial extent of the HZ for an Earth-like planet in a Keplerian orbit of increasing eccentricity around a star with solar luminosity. Abscissae: effective circular semi-major axis $a_{\rm eff} = a(1 - e^2)^{1/4}$ defined in Section 4.3.1. Left panel: habitability h; right panel: continuous habitability h_c (see Section 3.2). Model parameters are the same as in Figure 6.

(A color version of this figure is available in the online journal.)

presented in Figure 2 of Williams & Pollard (2002) and Figure 3 of Dressing et al. (2010); temperature differences are present, but generally lower than 5 K.

For comparison with the habitability study of Dressing et al. (2010), we calculated the temporal habitability, $f_{\rm time}$, versus latitude in orbits of various eccentricities and increasing semi-major axis. In this way, we used our model to reproduce the left panel of Figure 7 of Dressing et al. (2010). In common with these authors we find that (1) the range of habitable latitudes shrinks as a increases and (2) the temporal habitability undergoes a transition from high to low values above a critical value of a (the "outer edge"). At variance with Dressing et al., we find (1) a slightly larger value of the outer edge (e.g., 1.17 AU instead of 1.12 AU for the case $e = 0.6$) and (2) a tail of low temporal habitability ($f_{\rm time} \lesssim 0.2$) outside the "edge."

4.3.2. Non-solar-type Stars

The luminosity, $L_\star$, and mass, $M_\star$, of the central star are free parameters of our climate model. In the simulations presented in this work, we have adopted the solar values $L_\star = L_\odot$ and $M_\star = M_\odot$. In principle, these values can be changed to calculate the habitability of planets orbiting stars different from the Sun. As far as the luminosity is concerned, it is not even necessary to repeat the calculations: one can scale the maps of habitability according to the level of insolation $q = L_\star/(4\pi a^2)$, as shown in the top horizontal axis of Figure 3. In addition, one could incorporate in a single parameter, $\langle q \rangle = L_\star/(4\pi a_{\rm eff}^2)$, all the observable quantities that determine the insolation, including the eccentricity. In practice, however, a change of luminosity implies a change of stellar mass and spectral type and therefore one should take into account the following effects before applying the present results to non-solar stars.

For a given value of semi-major axis, a, the orbital periods of planets in Keplerian orbits around stars with different masses will scale as $P \propto M_\star^{-1/2}$. As a consequence, for a given level of insolation, the climate simulation should be calculated at the proper value of $M_\star$ in order to use the correct orbital period. Only in this way is it possible to follow the temporal evolution of the planet temperature, properly taking into account the different timescales relevant to the climate system. Specifically, the orbital period determines the seasonal evolution of the incoming stellar radiation, while the relative proportion of oceans and lands govern the thermal inertia of the climate. For habitable

planets around stars more massive than the Sun, the orbital period is larger than the highest timescale of thermal inertia (that of the oceans). The opposite is true for habitable planets around stars with mass equal to or lower than the solar mass.

The extension of the EBM model to low-mass stars faces the problem of the tidal locking. The physical quantities in the zonal EBM are meant to be diurnal zonal averages. The diurnal average is appropriate if the rotation period is smaller than the orbital period ($P_{\rm rot} \ll P_{\rm orb}$) and therefore should not be employed when the planet is tidally locked to its central star ($P_{\rm rot} = P_{\rm orb}$). This fact limits the study of the habitability around the coolest stars (of M type), since in this case the HZ is generally so close to the star that the planet is expected to become tidally locked in the long term. This limitation does not affect the results that we have presented here, which refer to the habitability around stars with solar-type flux. The method that we use can be extended to stars cooler than the Sun, as long as the region of habitability is more distant than the tidal lock radius. According to previous calculations, the HZ lies beyond the tidal lock radius up to spectral type around mid-K (see, e.g., Figure 5 in Kasting & Catling 2003).

In addition to the mass and luminosity, the spectral type of the central star may affect our analysis in different ways, mainly because the diffusion equation (1) lacks an explicit treatment of the wavelength dependence of the physical quantities.

The spectral distribution of the stellar radiation can affect the albedo properties (Selsis et al. 2007). The prescriptions that we adopt to model the albedo are calibrated for the Earth and, implicitly, for a solar-type spectral distribution. As discussed above for the tidal locking problem, the conclusions that we derive can be extended to stars with a somewhat later spectral type. However, care should be taken in applying our results to M-type stars.

A further issue related to the wavelength dependence concerns the separation between the incoming radiation, S, and the outgoing radiation, I, in Equation (1). This formal separation is valid if the spectral distribution of these two terms is well separated in wavelength. This condition is well satisfied for solar-type stars since the radiation of a G2 star peaks at $\simeq 0.5\,\mu$m and that of a habitable planet ($T \sim 300$ K) at $\simeq 10\,\mu$m. For stars of later spectral type, the peak shifts to longer wavelengths, but the assumption is still reasonable (the radiation of a M5 star peaks at $\simeq 0.9\,\mu$m).
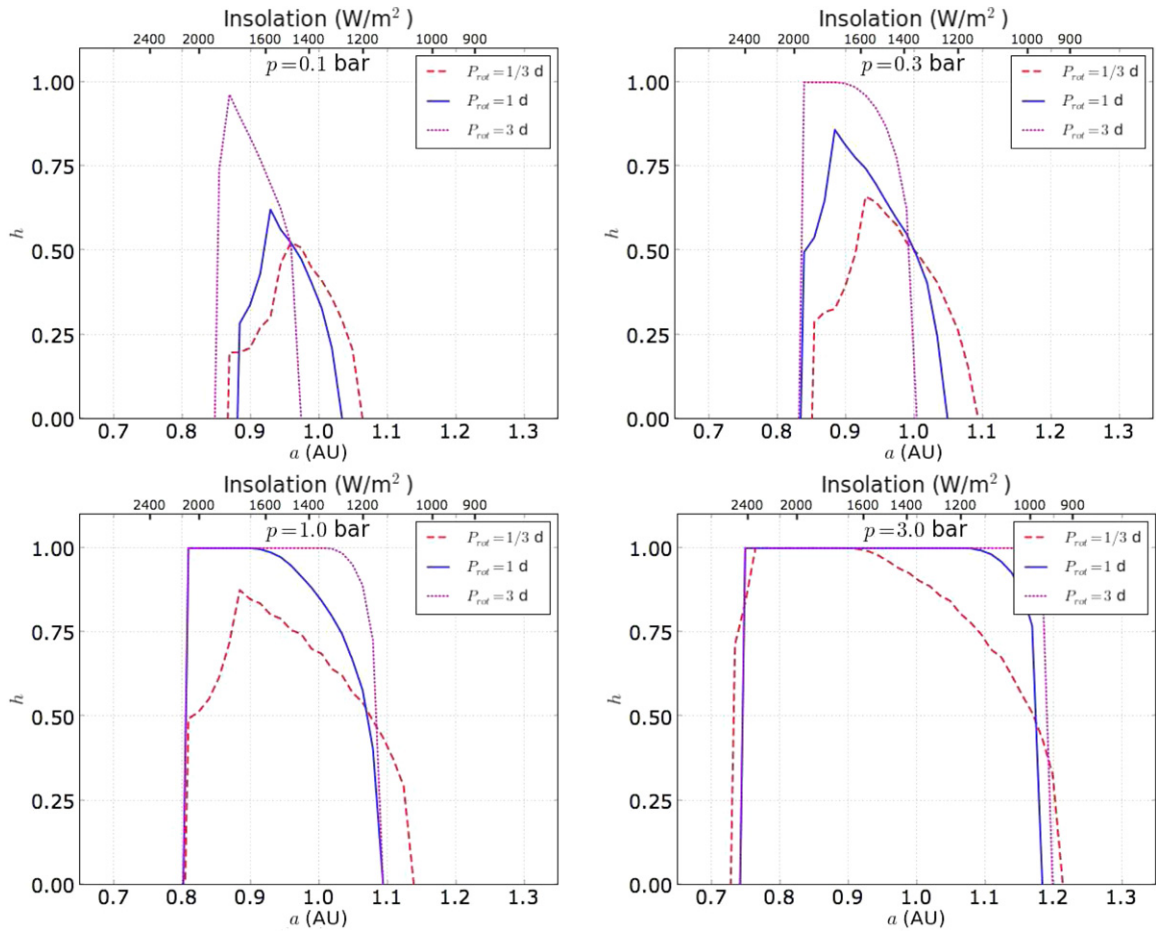
Figure 8. Fractional habitability, h, as a function of semi-major axis, a, for planets with rotation periods $P_{rot} = 1/3$, 1, and 3 days. Each panel shows the results obtained at a constant pressure p. The other parameters of the simulations are listed in Tables 2 and 3.

(A color version of this figure is available in the online journal.)

4.4. Effects of Parameters Unconstrained by Observations

At variance with the eccentricity and the stellar luminosity that can be derived from observational methods, many of the planetary parameters relevant for the climate and habitability are unconstrained by the observations of extrasolar planets. This is true, for instance, for rotation period, axis obliquity, planet geography, and surface albedo. Here we discuss how variations of such unconstrained quantities, in combination with variations of surface pressure, may affect the habitability of exoplanets.

4.4.1. Planet Rotation Period

In Figure 8, we plot the curves of habitability h versus a obtained for three rotation periods: $P_{rot} = 1/3$, 1, and 3 days (dashed, solid, and dotted curves, respectively). The four panels of the figure correspond to $p = 0.1$, 0.3, 1.0, and 3.0 bar, as indicated in the labels.

Planet rotation affects the habitability curves. The area subtended by the curves tends to increase and the shape tends to become top-flatted as the rotation period increases. The interpretation of this effect is as follows. An increase of P_{rot} yields a quadratic increase of the diffusion via Equation (A5) because $D \propto \Omega^{-2} \propto P_{rot}^2$. This effect tends to homogenize the surface temperature, particularly in the high-pressure regime (bottom panels), since the diffusion coefficient increases with p as well. An homogeneous temperature will yield abrupt transitions between a fully habitable and a fully non-habitable

situation, the extreme case considered here being the top-flatted, box-shaped habitability curve at $P_{rot} = 3$ days and $p = 3.0$ bar in the bottom right panel of the figure. At the other extreme of low rotation periods and low p, the habitability curves show instead a pronounced peak. Planets in these conditions experience significant variations in their habitability even with a modest change of a (i.e., of insolation). When the pressure is low (top-left panel) the habitability is relatively low. An increase of the rotation period helps to transport the horizontal heat and tends to raise the peak and increase the area subtended by the curve.

The comparison between the results shown in the four panels of Figure 8 indicates that the width and centroids of the curves of habitability tend to change together as pressure varies. All together, variations of the rotation period do not dramatically affect the general features of the pressure-dependent HZ.

Previous studies on the influence of the rotation period on planetary climate and habitability have been presented by SMS08. In common with these studies, we find a decrease in the planet temperature and habitability with increasing rotational velocity. However, our calculations do not yield the runaway transition to a snowball climate that was found by SMS08 by adopting $P_{rot} = 1/3$ day for the Earth. The different choice of the albedo prescriptions is a plausible reason for this different result. As one can see in the right panel of Figure 1, the albedo–latitude profile adopted by SMS08 is characterized by a sharp transition at high latitudes. Our model profile, which is in better agreement
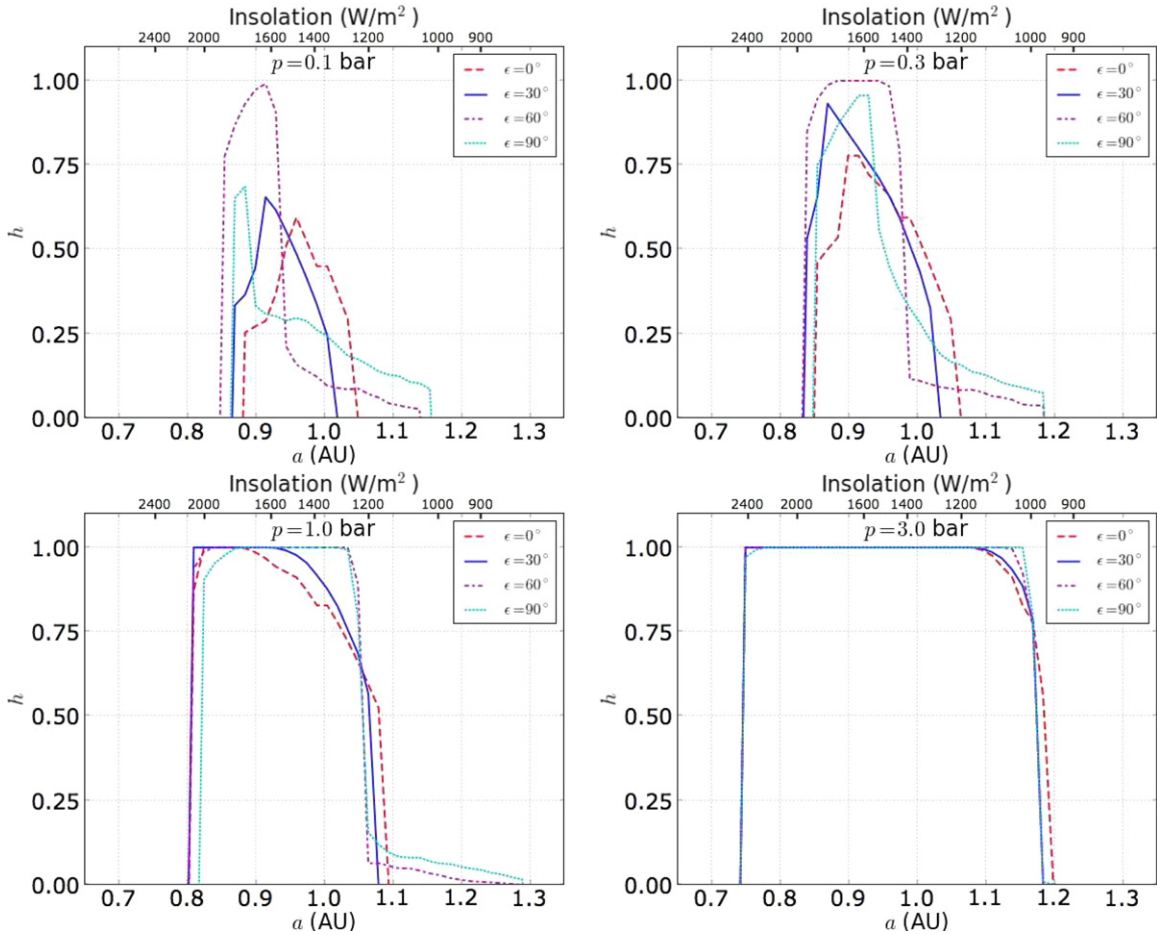
13

Figure 9. Fractional habitability, h, as a function of semi-major axis, a, for planets with axis obliquity $\epsilon = 0°$, $30°$, $60°$, and $90°$. Each panel shows the results obtained at a constant pressure p. The other parameters of the simulations are listed in Tables 2 and 3.

(A color version of this figure is available in the online journal.)

with the experimental data, does not show such a feature. The sharp transition of the albedo adopted by SMS08 is probably responsible for the very strong ice-albedo feedback found by these authors.

4.4.2. Axis Obliquity

In Figure 9, we plot the curves of habitability h versus a calculated at four values of obliquity: $\epsilon = 0°$, $30°$, $60°$, and $90°$ (dashed, solid, dash-dotted, and dotted curves, respectively). As in the previous figure, the four panels correspond to $p = 0.1$, 0.3, 1.0, and 3.0 bar.

The curves of habitability show strong variations with obliquity, in particular when the pressure is low. The general trend, at all pressures, is that the habitability increases with increasing ϵ when the obliquity is low ($\epsilon \lesssim 60°$) and decreases with increasing ϵ when the obliquity is high ($\epsilon \gtrsim 90°$). This complex behavior can be explained in the following way. The configuration at $\epsilon = 0°$ favors the formation of permanent ice caps in the polar regions, where the star is always at large zenith distance. As the obliquity starts to increase from zero, a larger fraction of polar regions undergo a period of stellar irradiation at low zenith distance in some phase of the orbit. This tends to reduce the ice caps and therefore to increase the habitability. However, when the obliquity becomes quite large, a permanent ice belt starts to build up in the equatorial zones, leading to a decrease in the habitability. To understand why the equator is colder than the poles we consider the extreme case $\epsilon = 90°$. In this case,

the maximum insolation of a polar region occurs when the pole faces the star; the instantaneous insolation at the pole does not change during the planet rotation, so that the mean diurnal insolation is $S = q$. The maximum insolation of an equatorial region instead occurs when the rotation axis is perpendicular to the star–planet direction. In this case, the instantaneous insolation at the equator undergoes the night–day cycle and the mean diurnal flux is $S = q/\pi$ (see Equation (A22) for this specific configuration, in which $\delta = 0$, $\varphi = 0$, and $H = \pi/2$). Our calculations indicate that the equatorial zones start to build up permanent ice when the obliquity increases from $\epsilon = 60°$ to $\epsilon = 90°$. The exact seasonal evolution is strongly dependent on the thermal inertia of the climate components.

The formation of an equatorial ice belt was first predicted by WK97 for the case $\epsilon = 90°$ and $p = 1$ bar. Our calculations indicate that the effect is stronger at lower pressures. The obliquity effects tend to disappear as the pressure increases. The bottom panels of Figure 9 show that at $p = 1$ bar, the variations are moderate and at $p = 3$ bar, the influence of obliquity becomes modest. This is due to the high efficiency of the horizontal transport at high p, which tends to cancel temperature gradients on the planet surface, preventing the formation of polar ice caps or an equatorial ice belt at extreme values of obliquity.

The width and centroids of the curves of habitability calculated at different obliquities tend to change together as pressure varies in the four panels of Figure 9. In this respect, we can
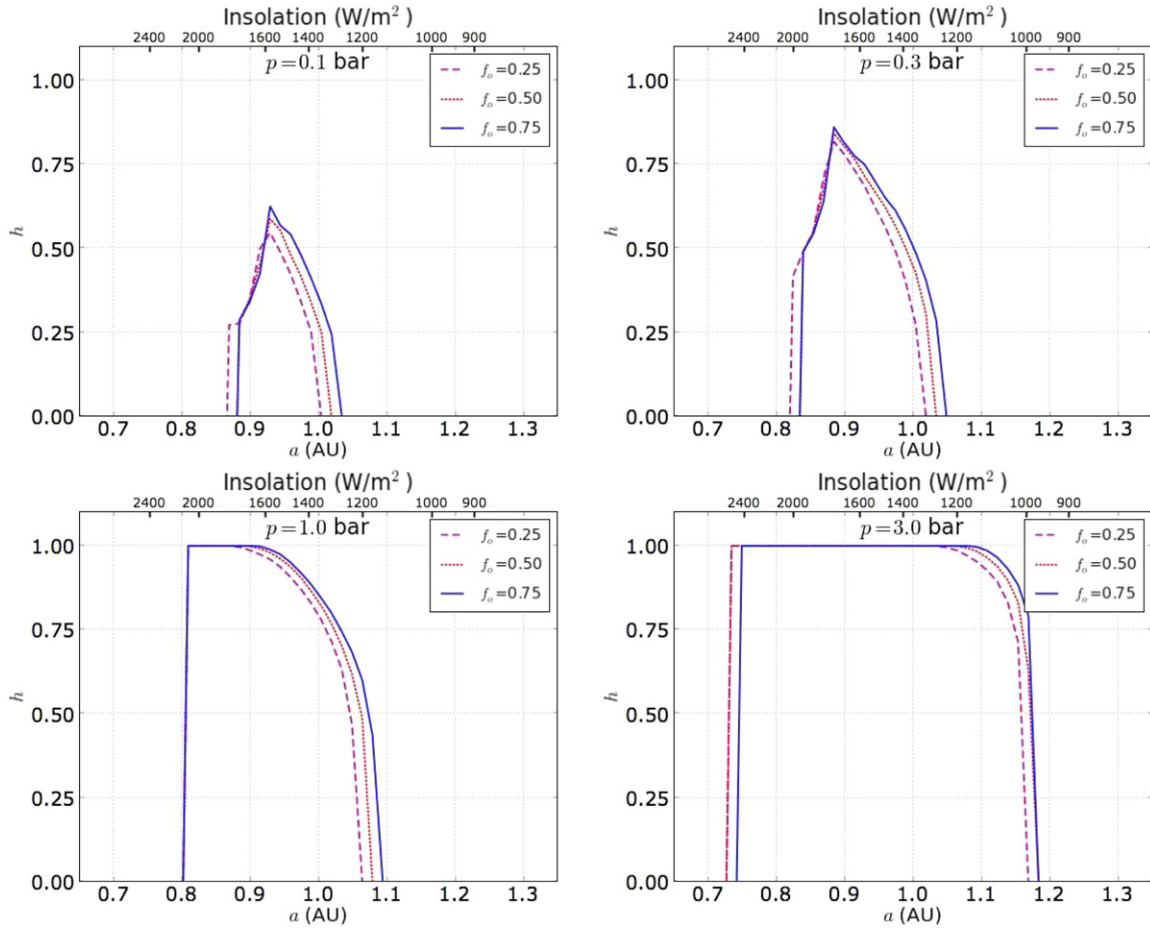
Figure 10. Fractional habitability, h, as a function of semi-major axis, a, for planets with ocean fractions $f_o = 0.25$, 0.50, and 0.75. Each panel shows the results obtained at a constant pressure p. The other parameters of the simulations are listed in Tables 2 and 3.

(A color version of this figure is available in the online journal.)

conclude, as in the case of the rotation period, that variations of the obliquity do not affect the overall characteristics of the pressure-dependent HZ.

Previous studies on the effects of obliquity have been performed by WK97 and Spiegel et al. (2009, hereafter SMS09). For comparison with WK97, we calculated the zonal surface temperature, T, as a function of orbital longitude, L_S, for an Earth with obliquity $\epsilon = 90°$. By considering the temperatures in five latitude zones centered on latitudes $-85°$, $-45°$, $+5°$, $+45°$, and $+85°$, we obtain trends of zonal T versus L_S very similar to those shown in Figure 1(B) of WK97, with temperature differences generally below 10 K.

For comparison with SMS09, we calculated the temperature–latitude profile of a planet with the same north polar continent considered by these authors, for three different obliquities ($\epsilon = 23°.5$, $60°$, and $90°$). Our model predicts temperature–latitude profiles similar to those visible in Figure 8 of SMS09, with an important difference: in the case $\epsilon = 90°$ the temporal evolution that we find is similar to that found by SMS09 only in the first $\simeq 10$ orbits of the simulation. Afterward, a snowball transition starts to occur in the simulation of SMS09 (bottom-right panel of their Figure 8), but not in our simulation. This result confirms that our climate model is relatively stable against snowball transitions, as we have discussed at the end of Section 4.4.1. Apart from this fact, the influence of obliquity on climate predicted by our EBM is similar to that predicted by previous work.

4.4.3. Planet Geography

Climate EBMs incorporate planet geography in a schematic way, the main parameter being the zonal coverage of oceans, f_o, which at the same time determines the coverage of lands, $f_l = 1 - f_o$. To explore the effects of geography on habitability we performed two types of tests. First we compared planets with different global coverage of oceans keeping f_o constant in all latitude zones. Then we compared planets with a different location of continents (i.e., polar versus equatorial) keeping constant the global fraction of oceans.

The results of the first test are shown in Figure 10, where we plot the curves of habitability h versus a calculated at three values of ocean fraction: $f_o = 0.25$, 0.50, and 0.75 (dashed, dotted, and solid curves, respectively). Each panel shows the results obtained at a constant pressure $p = 0.1$, 0.3, 1.0, and 3.0 bar. Two effects are visible as the coverage of oceans increases: (1) the HZ tends to shift to larger distances from the star; (2) at low pressures ($p \lesssim 1$ bar) the habitability tends to increase. Both effects are relatively small, at least for the combination of parameters considered. The increase in the thermal inertia of the climate system with increasing global ocean fraction is the key to interpreting these results. At low pressure the high thermal inertia of the oceans tends to compensate the inefficient surface distribution of the heat typical of low-pressure atmospheres. At high pressure, the combination of a high thermal inertia with an efficient atmospheric diffusion

tends to give the same temperature at a somewhat smaller level of insolation.

To investigate the effects of continental/ocean distribution, we considered the three model geographies proposed by WK97: (1) present-day Earth geography, (2) equatorial continent, and (3) polar continent. In practice, each model is specified by a set of ocean fractions, f_o, of each latitude zone (Table III in WK97). The case (2) represents a continent located at latitudes $|\varphi| < 20°$ covering the full planet. The case (3) represents a polar continent at $\varphi \lesssim -30°$. The global ocean coverage is approximately the same ($\langle f_o \rangle \simeq 0.7$) in the three cases. As a result, we find that these different types of model geographies introduce modest effects on the habitability curves. The habitability of present-day and equatorial continent geography are essentially identical at all pressures. The polar continent geography is slightly less habitable. This is probably due to the combination of two factors that tend to form a larger ice cap in the presence of a polar continent: (1) ice on land has a higher albedo than ice on water and (2) the thermal capacity of continents is lower than that of oceans. In any case, the differences in habitability are small and tend to disappear at $p \gtrsim 3$ bar due to the fast rise of the horizontal heat transport.

4.4.4. Albedo of the Continents

Albedo variations can shift the location of the HZ, moving the HZ inward if the albedo increases, or outward if the albedo decreases. In our model, the albedos of the oceans, ice, and clouds are not free parameters since they are specified by well-defined prescriptions (Appendix A.4). The albedo of the lands, a_l, is instead a free parameter. In the simulations run to build the map of Figure 3, we kept a fixed value $a_l = 0.2$, representative of the average of Earth continents. In a generic planet, the albedo of lands can vary approximately between $\simeq 0.1$ and 0.35, depending on the type of surface. The lowest values are appropriate, for instance, for basaltic rocks or conifer forests, while the highest values for Sahara-like deserts or limestone; Mars sand has $\simeq 0.15$, while grasslands have $\simeq 0.2$ (Pierrehumbert 2010). Given this possible range of continental albedos, we have repeated our calculations for $a_l = 0.1$, 0.2, and 0.35. As a result, we find that the curve of habitability h versus a shifts closer to the star for $a_l = 0.35$ and away from the star for $a_l = 0.1$. The maximum shift between the extreme cases is $\simeq 0.03$ AU. The shape of the habitability curves is virtually unaffected by these changes.

4.4.5. Surface Gradient of Latitudinal Heat Transport

With our formulation of the diffusion coefficient, we can investigate how planetary habitability is influenced by variations of the heat transport efficiency. In practice, this can be done by varying the parameter $\mathcal{R}$, that represents the ratio between the maximum and minimum value of the diffusion coefficient in the planet (Appendix A.2). The results shown in Figure 3 have been obtained for $\mathcal{R} = 6$, a value optimized to match Earth experimental data. We repeated our calculations for $\mathcal{R} = 3$ and $\mathcal{R} = 12$, keeping constant the fiducial value D_0, that represents the mean global efficiency of heat transport. As a result, we do not find any significant difference in planetary habitability either at high or low pressure. We conclude that the knowledge of the exact functional dependence on the latitude of the heat transport efficiency is not fundamental in predicting the properties of the HZ, at least with the simplified formalism adopted here that does not consider the circulation due to atmospheric cells.

4.4.6. Summary

The main effects of varying planetary parameters can be summarized as follows. As far as the *shape* of the habitability curves is concerned, the results at low pressure are quite sensitive to variations of rotation period, axis obliquity, and ocean coverage. Specifically, the habitability tends to increase with increasing rotation period, axis obliquity (up to $\epsilon \simeq 60°$), and ocean coverage. At high pressure, the shape of the habitability curves becomes insensitive to variations of these parameters. As far as the *location and radial extension* of the habitability curves is concerned, the results are modestly influenced by variations of planetary parameters, even at low pressure. Variations of the latitudinal/seasonal gradient of the heat transport efficiency do not affect the properties of the HZ. Albedo variations tend to shift the habitability curves without affecting their shape.

4.5. Final Considerations

4.5.1. The Edges of the Habitable Zone

Our calculations do not include the CO_2 climate stabilization mechanism considered in the classic HZ definition (Kasting et al. 1993). In principle, EBM models can be used to simulate the carbonate–silicate cycle that drives this mechanism (WK97). However, this choice is not practical when running thousands of simulations, as we do here, because the timescale of the CO_2 cycle is much larger than the timescale of convergence of the simulations. In addition, modeling the carbonate–silicate cycle requires ad hoc assumptions on the silicate weathering law and rate of CO_2 production by volcanos. At the present time it is not clear whether an active volcanism and tectonics, the ingredients required for the existence of the CO_2 cycle, are common in terrestrial planets. For planets that do have this cycle, the outer edge of the HZ would shift to larger values of semi-major axis than estimated here. For completeness we note that, if oceans are salty, the outer edge would shift in the same direction due to the lowering of the water freezing point.

As far as the inner edge is concerned, we adopt the water-loss limit criterion (3). At $p = 1$ bar, our inner edge is located at $a = 0.82$ AU, in the range of inner limits predicted by Selsis et al. (2007). However, the study of the latitude–temperature profiles obtained from our simulations shows the existence of cases that challenge the definition of the inner edge. Specifically, at low values of a and p in Figure 3, we find planets that are habitable, but have temperatures above the boiling point of water in some latitude zones. An example is shown in the right panel of Figure 5. The water reservoir of these type of planets is likely to undergo a complete evaporation in the long term. In fact, to avoid this fate, the continental distribution and axis obliquity should "conspire" to keep the oceans outside the boiling zone during all the planet's life. This in turn would require (1) a long-term mechanism of stabilization of the rotation axis and (2) the absence of tectonics drifts that, sooner or later, would build up a geography prone to evaporation. If the water reservoir is lost after an initial period of habitability, these planets match the definition of "Class II" habitats proposed by Lammer et al. (2009): bodies that possess Earth-like conditions in the early stages of evolution, but not in the long term. According to Lammer's scheme, Venus is a potential "Class II" object that may have lost its water by evaporation. In contrast with Venus, the planets that we find have a low boiling point, typical of low pressure, and can evaporate at a relatively cold global temperature. By excluding these "cold evaporating planets" from the map of Figure 3, the low-pressure inner edge would

shift to larger values of semi-major axis (e.g., from 0.87 AU to 0.93 AU at $p = 0.1$ bar).

4.5.2. Which Type of Life?

Even if the HZ of Figure 3 broadens with pressure, the type of life that can be expected to exist at a given level of pressure $p \gtrsim 1$ bar may be quite different, depending on the exact location of the planet in the plane (a, p). Indeed, most of the enlargement of the HZ at high pressures is due to the increasing fraction of regions with high temperatures lying above the isothermal contour $T_m = 60°$C (red curve in Figure 3). Taking terrestrial life as a reference, these regions would only be habitable by extremophilic organisms, specifically thermophiles and hyperthermophiles (see, e.g., Cavicchioli 2002). In fact, no terrestrial extremophile is known to exist above $\simeq 110$–$120°$C, the record being shared by a few archea living in oceanic hydrothermal vents (*Pyrolobus fumarii*, *Methanopyrus kandleri strain 116*, and *Strain 121*). On these grounds, it is debatable whether forms of life may exist beyond the isothermal contour $T_m = 120°$C (black curve in Figure 3). If we are interested in the distribution of mesophilic organisms, rather than in extremophiles, the HZ does *not* become larger with increasing pressure: for organisms adapted to a temperature within the range $0°C \lesssim T_m \lesssim 60°$C, the HZ shifts to larger distances from the central star as the pressure increases (region between the magenta and red curves in Figure 3).

As discussed above, the surface temperature becomes quite uniform when the pressure exceeds a few bars. The uniformity of the temperature at all latitudes and seasons means that habitable planets with high pressure can only host surface life adapted to a fine-tuned range of temperatures. As an example, the maximum temperature excursion at $p = 5$ bar at the outer edge of the HZ is $-12°C \leqslant T \leqslant +5°$C. This type of situation typical of high pressure is quite different from that of Earth, where the latitudinal and seasonal variations allow the presence of a wide diversity of surface life adapted to different temperatures. At lower pressures, the temperature excursions tend to become quite high allowing, in principle, an even broader gamut of surface life. In particular, terrestrial-type cryophilic organisms with optimal temperature $T < -15°$C would find a proper surface habitat only at low pressure ($p \lesssim 1$ bar) in the outermost regions of the HZ. However, at very low pressure the overall habitability severely decreases and becomes restricted to a narrow range of distances from the star.

5. CONCLUSIONS

We have implemented a one-dimensional EBM of planetary climate, based on the diffusion equation (1), aimed at exploring the surface habitability of extrasolar planets. Starting from the model prescriptions adopted in previous EBMs, our model contains new recipes for the diffusion coefficient, the outgoing IR flux, the albedo, the effective thermal capacity, and the ice and cloud cover. Our prescription for the diffusion coefficient introduces in a natural way seasonal and latitudinal variations in the efficiency of the heat transport. The formalisms adopted for the calculation of the albedo and effective thermal capacity are sufficiently general to be applied to planets with a variety of surface conditions. The recipe for the ice cover allows the formation of permanent ice caps or belts. The model parameters have been fine-tuned in such a way so as to reproduce the mean annual latitude profiles of the Earth temperature and albedo (Figure 1), as well as the seasonal variability of the temperature–latitude profiles (Figure 2).

As a first application of our model, we have investigated the habitability of planets with Earth-like atmospheric composition but different levels of surface pressure. The habitability is estimated on the basis of the pressure-dependent liquid water temperature range, taking into account the seasonal and latitudinal variations of the surface temperature. By running a large number of climate simulations with our EBM we have estimated the mean global annual temperature, T_m, and habitability, h, as a function of semi-major axis, a, and surface pressure, p. In this way, we have built up a habitability map (Figure 3) that represents the pressure-dependent HZ for planets with Earth-like atmospheres orbiting a solar-type star. The main results that we find can be summarized as follows.

1. The radial extent of the HZ increases with pressure, from $\Delta a = 0.18$ AU at $p = 1/3$ bar to $\Delta a = 0.43$ AU at $p = 3$ bar.
2. At a given value of semi-major axis a, or insolation, $q = L_\star/(4\pi a^2)$, the mean temperature and habitability tend to rise with increasing pressure (Figure 4).
3. Remarkable differences in surface temperature and habitability exist between the low- and high-pressure regimes, mainly because the range bracketed by extreme surface temperatures decreases with increasing pressure (Figure 4).
4. At low pressures ($p \lesssim 0.3$ bar) the habitability is generally low and varies with a. At high pressure ($p \gtrsim 1$ bar), the habitability is high and relatively constant inside the HZ.
5. In the temperature range suitable for terrestrial mesophilic organisms ($0°C \lesssim T_m \lesssim 60°$C), the HZ moves away from the star as pressure increases, rather than becoming broader.

The characteristics of the pressure-dependent HZ result from the complex interaction of physical effects that become stronger as the surface pressure increases. The main ones are the intensity of the greenhouse effect (recalling that we keep the atmospheric composition fixed), the efficiency of latitudinal heat transport, and the broadening of the temperature range of liquid water. The increase of the greenhouse effect bends the contours of equal planet temperature toward higher distances from the star as the pressure increases. The broadening of the liquid water range bends the inner edge of the HZ closer to the star as pressure increases. The rise of the latitudinal heat transport tends to yield uniform planet temperatures at high pressure.

The comparison of our boundaries of habitability with the limits of the classic HZ around a Sun-like star yields the following conclusions. Our inner edge, calculated for Earth-like pressure, cloudiness, and humidity, is located at $a = 0.82$ AU, in the range of the inner limits predicted by Selsis et al. (2007). Our outer edge, calculated for Earth-like atmospheric composition, lies at $a = 1.08$ AU, much closer to the star than the quoted outer limits of the classic HZ, which are estimated for CO_2-rich planetary atmospheres (Kasting et al. 1993; Selsis et al. 2007).

Thanks to the EBM capability of exploring the latitudinal and seasonal variations of the surface temperature we have found the following results.

1. The mean global planet temperature, T_m, is not a good indicator of habitability at low pressure. As an example, we find planets that are habitable even if T_m is well below the water freezing point (left panel of Figure 5). This result highlights the need of solving the latitude profile to properly characterize planetary habitability.
2. Habitable planets with zonal temperatures above the water boiling point may in principle exist (right panel of Figure 5). These cases are new candidate "Class II" habitats (Lammer

et al. 2009), i.e., bodies that become unsuitable to host life after an initial period of habitability.

Our results, calculated for circular orbits, can be extended to planets in Keplerian orbits with moderate eccentricity ($e < 0.5$), provided one uses the effective circular semi-major axis $a_{\rm eff} = a(1 - e^2)^{1/4}$ as a proxy of a. At higher eccentricities, however, the extent of the HZ shrinks considerably (Figure 7). In principle, our results can also be applied to planets orbiting stars different from the Sun, provided one uses the insolation $q = L_\star/(4\pi a^2)$ rather than the semi-major axis. In practice, there are several reasons, discussed in Section 4.3.2, why this type of generalization should be done with caution.

The potential effects on climate of physical quantities unconstrained by observations is a reason of concern in the study of exoplanets. Thanks to the flexibility of our EBM simulations we have explored how the habitability, and its dependence on pressure, can be influenced by changes of rotation period, axis obliquity, planet geography, and surface albedo. We find the following results.

1. The shapes of the curves of habitability h versus a are sensitive to variations of planetary parameters at low pressure, but not at high pressure.
2. The general location and radial extension of the pressure-dependent HZ are modestly influenced by planetary parameters.

In conclusion, climate EBMs offer a powerful tool to determine the range of stellar, orbital, and planetary parameters that satisfy the liquid water criterion in exoplanets. The possibility of investigating seasonal and latitudinal variations of the surface temperature offers a significant insight on the habitability and its long-term evolution, as well as on the possible type of life that might exist on the planetary surface. These type of studies will help to optimize the selection of targets in future searches for biomarkers in extrasolar planets.

APPENDIX

MODEL PRESCRIPTIONS

We present the formalism adopted to model the physical quantities C, D, I, A, and S that appear in the diffusion equation (1). General introductory remarks on these quantities are given in Section 2. Further details can be found in the literature cited in the text.

A.1. Effective Thermal Capacity, C

The term C represents the thermal inertia of the atmospheric and surface layers that contribute to the surface energy budget. For a layer with density ρ, specific heat capacity $c_{\rm p}$, and depth $\Delta\ell$, the effective thermal capacity is $C = \rho\, c_{\rm p}\, \Delta\ell$. In a planet with oceans, the surface oceanic layers mixed by the winds provide the main contribution to the thermal

inertia. A wind-mixed ocean layer with $\Delta\ell = 50$ m has $C_{\rm ml50} = 210 \times 10^6$ J m^{-2} K^{-1} (WK97). Also the contribution of the atmosphere can be expressed in terms of an equivalent mixed ocean layer. For the Earth atmosphere, the equivalent ocean depth is 2.4 m (Pierrehumbert 2010), corresponding to $C_{\rm atm,\circ} = 10.1 \times 10^6$ J m^{-2} K^{-1}. For other planetary atmospheres the thermal inertia will scale as

$$\left(\frac{C_{\rm atm}}{C_{\rm atm,\circ}}\right) = \left(\frac{c_{\rm p}}{c_{\rm p,\circ}}\right)\left(\frac{p}{p_\circ}\right), \qquad (A1)$$

where $c_{\rm p}$ and p are the specific heat capacity and total pressure of the atmosphere, respectively (Pierrehumbert 2010). The effective heat capacity of the solid surface is generally negligible. As a representative value, a layer of rock or ice with $\Delta\ell = 0.5$ m yields a contribution $C_{\rm solid} \simeq 1 \times 10^6$ J m^{-2} K^{-1}. This term, even if small, is not negligible in planets without oceans and with very thin atmospheres. On the basis of the above considerations, we adopt

$$C_o = C_{\rm ml50} + C_{\rm atm}$$
$$C_l = C_{\rm solid} + C_{\rm atm} \qquad (A2)$$

for the thermal inertia of the atmosphere over oceans and lands, respectively. For ices not undergoing liquid–solid transition, we adopt $C_i = C_l$. In the temperature range $263 < T < 273$, we add an extra contribution to the thermal inertia of ice to take into account the latent heat of phase transition. In practice, based on similar recipes adopted by North et al. (1983) and WK97, we adopt $C_i = C_l + C_{\rm ml50}/5$.

The mean effective thermal capacity of each latitude zone is calculated using as weighting factors the coverage of oceans, f_o, and continents, $f_l = 1 - f_o$. The expression that we use

$$C = f_l[(1 - f_i)\,C_l + f_i\,C_i] + f_o[(1 - f_i)C_o + f_i\,C_i] \quad (A3)$$

takes into account the ice coverage, f_i, estimated as explained in Appendix A.6.

All together, our values of thermal capacity are very similar to those adopted by WK97 and SMS08, with the exception of $C_{\rm atm,\circ}$, which is about twice in our case. Attempts to use higher values of the ocean capacity previously proposed by North et al. (1983) and representative of a 75 m deep wind-mixed ocean layer, yield a worse match between the model predictions and the Earth experimental data.

A.2. Diffusion Coefficient, D

The horizontal transport of heat on the planet surface is mainly due to the general circulations and the related instabilities of the ocean and the atmosphere, which are governed by many factors. The most relevant are the physical and chemical properties of the atmosphere and oceans, the presence of Coriolis force induced by the planet rotation, and the topography of the planet surface. Since EBMs are zonally averaged, longitudinal variations of the heat transport are not considered. Even so, it is extremely difficult to model all the factors that govern the latitudinal transport. To keep low the computational cost, EBMs incorporate the efficiency of the transport into a single quantity, namely the diffusion coefficient D, even though representing latitudinal heat transport by a diffusive term is, in itself, a gross simplification. In previous EBM work, this term has been parameterized using a scaling law that takes into account the dependence of the diffusion coefficient on the main physical

quantities involved in the latitudinal transport. The relation proposed by WK97,

$$\left(\frac{D}{D_\circ}\right) = \left(\frac{p}{p_\circ}\right)\left(\frac{c_p}{c_{p,\circ}}\right)\left(\frac{m}{m_\circ}\right)^{-2}\left(\frac{\Omega}{\Omega_\circ}\right)^{-2}, \qquad (A4)$$

gives D as a function of atmospheric pressure, p, specific heat capacity, c_p, mean molecular weight, m, and angular velocity of planet rotation, Ω. All these quantities are scaled with respect to the reference Earth values. A discussion of the physics underlying this relation can be found in WK97. A number of recent applications of EBM to exoplanet climates have adopted the same relation (SMS08; Dressing et al. 2010). We refer to these papers for cautionary remarks regarding the limits of validity of the scaling relation $D \propto \Omega^{-2}$.

In our work, we address an intrinsic limitation of the above formulation, namely the fact that, once the planet parameters are specified, D is constant in latitude and time. This approximation is too crude because Earth's latitudinal transport is driven by atmospheric convective cells characterized by a latitudinal pattern with seasonal variations. As a consequence, in real planets the efficiency of the diffusion will vary in latitude and time. Here we propose a formalism that introduces latitudinal and seasonal variations of D related to the stellar zenith distance. This formalism can be applied to a generic planet.

Most of the latitudinal heat transport is carried out by the circulation that takes place in the atmospheric convective cells. On Earth, the most notable of these features are the two Hadley cells that depart from the intertropical convergence zone (ITCZ) and produce the net effect of a polarward transport. The position of the Hadley cells shifts during the year, influenced by the solar zenith distance. This is demonstrated by the seasonal shift of the ITCZ, which moves to higher latitudes in the summer hemisphere. Since the Hadley cells yield the largest contribution to the latitudinal heat transport, we conclude that the maximum efficiency of this type of transport is larger when the zenith distance $Z_\star$ is smaller. Inspired by this behavior, and without making specific assumptions on the systems of atmospheric cells that may be present in a generic planet, we have introduced a dependence of the diffusion coefficient on $\mu = \cos Z_\star$. More specifically, we assume that D scales with the mean diurnal value $\overline{\mu}$, derived from Equation (A23). From this equation and Equation (A25) one can see that $\overline{\mu}$ depends on the latitude, φ, and the obliquity of the axis of rotation, ε; it also depends on the time of the year, t, which determines the seasonal value of $\delta_\star$ and $\lambda_\star$. Therefore, by assuming a dependence $D = D(\overline{\mu})$ we introduce, in practice, a dependence on φ, t and ε. To incorporate this effect in the EBM prescriptions, we adopt the following expression:

$$\left(\frac{D}{D_\circ}\right) = \zeta_\varepsilon(\varphi, t)\left(\frac{p}{p_\circ}\right)\left(\frac{c_p}{c_{p,\circ}}\right)\left(\frac{m}{m_\circ}\right)^{-2}\left(\frac{\Omega}{\Omega_\circ}\right)^{-2}, \quad (A5)$$

where $\zeta_\varepsilon(\varphi, t)$ is a modulating factor that scales linearly with $\overline{\mu}$. This factor is normalized in such a way that the mean global annual value of D equals that given by the scaling law (A4). Thanks to this fact, we can make use of the previous studies of the diffusion coefficient, as far as the dependence on p, c_p, m, Ω is concerned, and of our own formalism, as far as the dependence on φ, t, and ε is concerned. We now show how the modulating factor $\zeta_\varepsilon(\varphi, t)$ can be expressed as a function of a single parameter, $\mathcal{R}$, that represents the ratio between the maximum and minimum values of the diffusion coefficient in the planet.

A.2.1. The Modulating Factor ζ

To obtain an expression for the modulating factor, ζ, we use the following defining conditions: (1) ζ scales linearly with $\overline{\mu}$; and (2) ζ is normalized in such a way that its mean global annual value is $\langle \zeta_\varepsilon(\varphi, t) \rangle = 1$. The first condition translates into

$$\zeta_\varepsilon(\varphi, t) = c_0 + c_1\, \overline{\mu}_\varepsilon(\varphi, t), \qquad (A6)$$

where c_0 and c_1 are two constants. The second condition becomes

$$\langle \zeta_\varepsilon(\varphi, t) \rangle = c_0 + c_1 \langle \overline{\mu}_\varepsilon(\varphi, t) \rangle = 1, \qquad (A7)$$

where

$$\langle \overline{\mu}_\varepsilon(\varphi, t) \rangle = \frac{\int_0^P dt \int_{-\pi/2}^{+\pi/2} d\varphi \cos\varphi\, \overline{\mu}_\varepsilon(\varphi, t)}{\int_0^P dt \int_{-\pi/2}^{+\pi/2} d\varphi \cos\varphi}. \qquad (A8)$$

To determine c_0 and c_1, we need an additional relation between these two constants. For this purpose, we follow an approach similar to that of North et al. (1983), who adjusted the diffusion coefficient to be three times as large at the equator as it is at the poles. In the framework of our formulation, this condition would be expressed in the form $\mathcal{R} = 3$, where

$$\mathcal{R} = \frac{[\zeta_\varepsilon(\varphi, t)]_{max}}{[\zeta_\varepsilon(\varphi, t)]_{min}} \qquad (A9)$$

is the ratio between the maximum and minimum values of the modulation factor in any latitude zone and at any orbital phase. The above condition is equivalent to

$$\mathcal{R} = \frac{c_0 + c_1\,[\overline{\mu}_\varepsilon(\varphi, t)]_{max}}{c_0 + c_1\,[\overline{\mu}_\varepsilon(\varphi, t)]_{min}} = \frac{c_0 + c_1\,[\overline{\mu}_\varepsilon(\varphi, t)]_{max}}{c_0}, \quad (A10)$$

where we have used the fact that $[\overline{\mu}_\varepsilon(\varphi, t)]_{min} = 0$ since $\overline{\mu} = 0$ in the zones where the star lies below the horizon during a period of rotation. We treat $\mathcal{R}$ as an input parameter of the model used to estimate c_0 and c_1. By combining Equations (A7) and (A10), it is easy to show that

$$c_1 = \left(\frac{[\overline{\mu}_\varepsilon(\varphi, t)]_{max}}{\mathcal{R} - 1} + \langle \overline{\mu}_\varepsilon(\varphi, t) \rangle\right)^{-1} \qquad (A11)$$

and

$$c_0 = c_1 \times \frac{[\overline{\mu}_\varepsilon(\varphi, t)]_{max}}{\mathcal{R} - 1}. \qquad (A12)$$

The quantities $[\overline{\mu}_\varepsilon(\varphi, t)]_{max}$ and $\langle \overline{\mu}_\varepsilon(\varphi, t) \rangle$ are calculated given the obliquity ε. To compute the double integral in Equation (A8) we use the expression of $\overline{\mu}$ given in Equation (A23), with the condition $\overline{\mu} = 0$ when $H \leqslant 0$, i.e., when the Sun is below the local horizon for a complete rotation of the planet.

A.2.2. Calibration of $\mathcal{R}$

The parameter $\mathcal{R}$ was tuned to improve the match between the observed and predicted temperature–latitude profile of Earth. The observed profile shows two features that are quite difficult to reproduce with a simple EBM. One is the almost flat temperature profile within the tropical belt, the other is the sharp temperature drop at latitude $\varphi \simeq -60°$ (Figures 1 and 2). By increasing $\mathcal{R}$ we are able to improve the match to both features. We obtain the best results by adopting $\mathcal{R} = 6$. The temperature profile that we obtain is flatter at the tropics than in previous work (Figure 1);

the temperature drop at $\varphi \simeq -60°$ is reproduced particularly well for the months of June, July, and August (see the case of July in Figure 2). The disagreement between the observed and modeled profiles at $\varphi < -60°$ is probably due to the particular characteristics (e.g., the high surface elevation) of Antarctica.

A.3. The Outgoing Long-wavelength Radiation, I

In climate EBMs, the OLR is usually expressed as a function of the temperature. In our problem, we are interested in probing variations of total pressure and therefore we need an expression $I = I(T, p)$. The pressure dependence of the OLR enters through the infrared optical depth of the atmosphere, τ_{IR}, which governs the intensity of the greenhouse effect. In principle, one may expect a strong dependence of τ_{IR} on p as a result of two effects. First, in a planetary atmosphere $\tau_{IR} = \kappa_{IR}\, p/g$, where κ_{IR} is the total absorption coefficient and g is the gravitational acceleration. Second, in the range of planetary surface pressures, κ_{IR} is dominated by collisional broadening, which introduces a linear dependence on p of the widths of the absorption lines (Pierrehumbert 2010; Salby 2012). In the absence of line saturation, κ_{IR} should therefore increase linearly with p. All together, one might expect $\tau_{IR} = \kappa_{IR}\, p/g \propto p^2$. In practice, however, the rise of the optical depth is milder because (1) the absorptions of different species may overlap in wavelength, (2) lines are partly saturated, and (3) the amount of water vapor, which is an important contributor to κ_{IR}, is independent of p. Given the complex interplay of these factors, it is not possible to derive a simple analytical function $\tau_{IR} = \tau_{IR}(T, p)$. Therefore, in order to obtain $I = I(T, p)$, we performed a series of radiative calculations and tabulated the results as a function of T and p.

We used standard radiation models developed at the National Center for Atmospheric Research (NCAR), as part of the Community Climate Model (CCM) project. The calculations were performed in a column radiation model scheme for a cloud-free atmosphere (Kiehl & Briegleb 1992). We used the set of routines CliMT (Pierrehumbert 2010; Caballero 2012), adopting Earth's value of surface gravitational acceleration. We varied p while keeping the mixing ratios of non-condensable greenhouses gases (CO_2 and CH_4) equal to Earth's values. The reference values of total pressure and partial pressure of greenhouse gases are shown in Tables 1 and 2. The contribution of water vapor was parameterized through the relative humidity, rh, as we explain below. In the regime of high temperatures, we increased the resolution of the vertical strata (up to 10,000), in order to better track the water vapor in the higher atmospheric levels. To test the radiative calculations in the regime of very low pressure (i.e., negligible atmospheric greenhouse), we compared the predicted OLR with the blackbody radiation calculated at the planet surface. As expected, the results are identical as long as water vapor is negligible.

To calibrate the OLR for the case of Earth, we used as a reference the mean annual Earth OLR measured with the *Earth Radiation Budget Satellite* (*ERBE*) satellite (online material published by Pierrehumbert 2010). In practice, we combined two ERBE data sets—i.e., the OLR versus latitude and the surface temperature versus latitude—to build a set of OLR data versus temperature. These experimental data are shown with crosses in Figure 11. To test different types of models, we then used the CCM to calculate the clear-sky OLR as a function of temperature for different values of relative humidity ($rh = 0.1$, 0.5, and 1.0). We then subtracted 28 W m^{-2} to the clear-sky results to take into account the mean global long-wavelength forcing of the clouds on Earth (Pierrehumbert 2010).
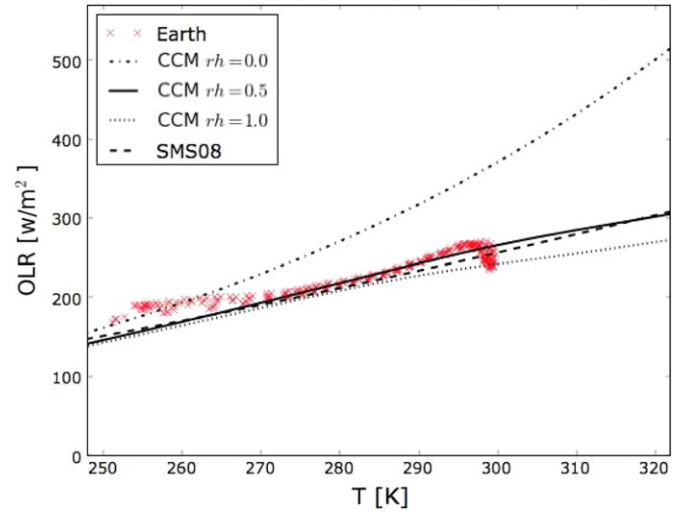

Figure 11. Comparison of radiative calculations and experimental data of the OLR of Earth. Crosses: mean annual data obtained from the ERBE satellite for the years 1985–1988. CCM radiative calculations for an Earth-type atmosphere with relative humidity $rh = 0$, 0.5, and 1.0 are shown as dot-dashed, solid, and dotted curves, respectively, after subtraction of the mean global long-wavelength cloud forcing (see Appendix A.3). Dashed curve: OLR model adopted by SMS08.

(A color version of this figure is available in the online journal.)

The three CCM curves resulting for $rh = 0.1$, 0.5, and 1.0 are shown in Figure 11. The curve obtained for $rh = 0.5$ (solid line) gives the best match to the experimental data and is very similar to the OLR adopted by SMS08 and SMS09 (dashed line). Based on these results, we adopted $rh = 0.5$ in our model. For applications to planets with cloud coverage $\langle f_c \rangle$ different from that of Earth, $\langle f_{c,\circ} \rangle$, we subtract $28\,(\langle f_c \rangle / \langle f_{c,\circ} \rangle)$ W m^{-2} to the clear-sky OLR obtained from the radiative calculations.

A.4. Albedo, A

In the formulation of SMS08, the albedo is an analytical function of the temperature, which, in practice, considers two types of surfaces: with ice and without ice. In our work, we employ a formalism that can be applied to planets with any type of surface characteristics. For each latitude zone we calculate a mean albedo by weighting the contributions of continents, a_l, oceans, a_o, clouds, a_c, ice on continents, a_{il}, and ice on oceans, a_{io}. The weighting factors are the zonal coverage of oceans, f_o, and continents, f_l; within oceans and continents we separate the contribution of ice, f_i; the cloud coverage on water, land, and ice is specified by the parameters f_{cw}, f_{cl}, and f_{ci}, respectively. In this way, we obtain

$$
\begin{aligned}
a_s = f_o\{&(1 - f_i)[a_o(1 - f_{cw}) + a_c f_{cw}] \\
&+ f_i[a_{io}(1 - f_{ci}) + a_c f_{ci}]\} \\
+ f_l\{&(1 - f_i)[a_l(1 - f_{cl}) + a_c f_{cl}] \\
&+ f_i[a_{il}(1 - f_{ci}) + a_c f_{ci}]\}.
\end{aligned} \quad (A13)
$$

In this equation, we have omitted for simplicity the latitude dependence of the zonal coverage of oceans and lands. This formulation of the surface albedo is similar to that adopted by WK97. At variance with that work, we consider the ice on continents (not only on oceans) and variable cloud cover. Only a few parameters in the above expression are free. Most of the albedo parameters are estimated with specific prescriptions that

we describe below. The zonal coverages of oceans, lands, ice, and clouds are described in Appendix A.6. In practice, only the zonal fraction of oceans, f_o, and the continental albedo, a_l, are free parameters.

A.4.1. Albedo Parameters

For the albedo of the continents, we adopt $a_l = 0.2$, the same value used by WK97, as a representative value of the Earth continents. For other planets we treat a_l as a free parameter that can typically vary between 0.1 and 0.35 (see Section 4.4.4).

The albedo of the oceans plays a crucial role in the estimate of a_s. The ocean reflection depends on the zenith distance of the star, $Z_\star$, that the EBM provides self-consistently as a function of time and latitude. WK97 adopted the Fresnel formula (Kondratyev 1969) to model the ocean reflectivity. However, the Fresnel formula is an ideal approximation valid for smooth surfaces while the actual sea level is never ideally smooth. For this reason we opted for a function calibrated with experimental data (Briegleb et al. 1986; Enomoto 2007):

$$a_o = \frac{0.026}{(1.1\,\mu^{1.7} + 0.065)} + 0.15(\mu - 0.1)\,(\mu - 0.5)\,(\mu - 1.0), \quad (A14)$$

where $\mu = \cos Z_\star$ is calculated with Equation (A20). Compared to the Fresnel formula, this expression gives very similar results at $Z_\star \lesssim 40°$, but a less steep, more realistic, rise at high values of zenith distance (Enomoto 2007).

For the albedo of ice over lands and ocean we adopted $a_{il} = 0.85$ and $a_{io} = 0.62$, respectively. The existence of a difference between these two types of albedo has been documented in previous work (Kondratyev 1969; Pierrehumbert 2010). By adopting a high albedo for ice over continents, we improve the modelization of the Earth climate on Antarctica, which is a critical point of EBMs (see Figure 1 and Section 2.3).

The cloud albedo, a_c, depends on the microphysical properties and geometrical dimensions of the clouds, which determine their optical properties. For a cloud of given optical thickness, the albedo increases with increasing stellar zenith angle, $Z_\star$, which elongates the slant optical depth (Salby 2012). A linear dependence of a_c on $Z_\star$ was reported by Cess (1976) for a set of data representative of the Earth cloud albedos. On the basis of that result, WK97 adopted $a_c = \alpha + \beta Z_\star$ and tuned the parameters α and β in such a way so as to match the total Earth albedo with their model. Since this tuning yields $\alpha < 0$, a problem with this formalism is that the cloud albedo vanishes at low zenith distances and becomes negative at $Z_\star = 0$. We expect, instead, a minimum value of cloud albedo to exist at $Z_\star = 0$, corresponding to the minimum vertical thickness of the cloud. For this reason, in our work we adopt the same parameterization, but with a minimum value of cloud albedo at low zenith distances, a_{c0}. In practice, we use the expression

$$a_c = \max\{a_{c0}, [\alpha + \beta Z_\star]\}. \quad (A15)$$

We estimate α and β by requiring the relation $\alpha + \beta Z_\star$ to yield a good fit to Cess data. We then tune a_{c0} in such a way so as to match the total Earth albedo with our model. In this way we obtained $\alpha = -0.07$, $\beta = 8 \times 10^{-3}(°)^{-1}$, and $a_{c0} = 0.19$.

A.5. Incoming Stellar Radiation, S

The incoming stellar radiation is calculated as the diurnal average

$$S = \frac{\int_0^{2\pi} s(t_\star)\,dt_\star}{\int_0^{2\pi} dt_\star} \quad (A16)$$

of the stellar flux $s(t_\star)$ incident on the planet at latitude φ, where $t_\star$ is the instantaneous hour angle of the star measured in angle units from the local meridian. To estimate $s(t_\star)$ we proceed as follows. At the time t, the planet is located at a distance $r = r(t)$ from its star. The stellar flux at such distance is

$$q(r) = \frac{L_\star}{4\pi r^2}, \quad (A17)$$

where $L_\star$ is the bolometric luminosity of the star. If we call $Z_\star$ the stellar zenith angle, the instantaneous flux at the planet surface is

$$s(t_\star) = \begin{cases} \tau_a\, q(r)\, \cos Z_\star & \text{if}\,|t_\star| < H \\ 0 & \text{if}\,|t_\star| \geqslant H \end{cases} \quad (A18)$$

where τ_a is the short-wavelength transmissivity of the atmosphere and H is the half-day length. By definition, $-H \leqslant t_\star \leqslant +H$ represents the portion of rotation period during which the star stays above the horizon. The half-day length in radians can be estimated from the expression (WK97)

$$\cos H = -\tan \varphi \tan \delta (0 < H < \pi). \quad (A19)$$

The flux $s(t_\star)$ is null when $|t_\star| \geqslant H$ because in this case the star is below the horizon ($Z_\star \geqslant \pi/2$). The zenith distance, $Z_\star$, is related to the latitude, φ, the stellar declination, $\delta_\star$, and the hour angle, $t_\star$, by means of the equation

$$\cos Z_\star = \sin \varphi\, \sin \delta_\star + \cos \varphi\, \cos \delta_\star\, \cos t_\star. \quad (A20)$$

With the above relations, we can calculate the average (A16) along circles of constant latitude. In these circles, the terms $\sin \varphi$ and $\cos \varphi$ are constant in the integration. Also the declination $\delta_\star = \delta_\star(t)$ and the flux $q(r) = q(r[t])$ can be treated as constants if the rotation period is much smaller than the orbital period, i.e., if

$$P_{rot} \ll P_{orb}. \quad (A21)$$

With these assumptions, if the atmosphere is transparent in the short wavelength range ($\tau_a = 1$), it is easy to show that

$$S = \frac{q(r)}{\pi}\,(H \sin \varphi\, \sin \delta_\star + \cos \varphi\, \cos \delta_\star\, \sin H). \quad (A22)$$

In a similar fashion, by defining $\mu = \cos Z_\star$, it is possible to calculate the mean diurnal value of μ when the star is above the horizon, $\overline{\mu} = \int_{-H}^{H} \mu\, dt_\star / \int_{-H}^{H} dt_\star$, and obtain the relation

$$\overline{\mu} = \sin \varphi\, \sin \delta_\star + \cos \varphi\, \cos \delta_\star\, \frac{\sin H}{H} \quad (A23)$$

that we use in our formulation of the diffusion coefficient.

Once we have obtained the diurnal average S, we calculate its temporal variation in the course of the orbital period, $S = S(t)$. The time t specifies the planet position along the orbit and $S = S(t)$ represents the seasonal evolution of the flux at a given latitude. The only quantities that depend on t in Equation (A22)
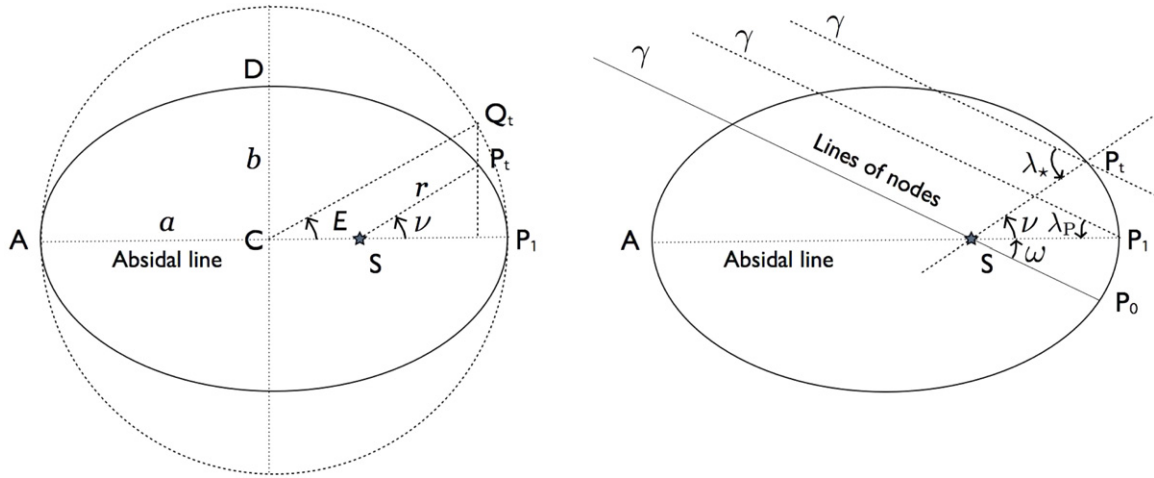
Figure 12. Orbital elements used in the derivation of the incoming stellar radiation (Appendix A.5). The ellipsis represents the planet orbit; S is the star, located at one focus of the ellipsis; P_t is the position of the planet at time t; P_1 is the planet at the pericenter; the absidal line connects the pericenter to the apocenter, A. The semi-major axis is $a = AC$; the semi-minor axis is $b = CD = a\sqrt{(1 - e^2)}$. Left panel: elements used to demonstrate relations (A24) and (A27); E is the *eccentric anomaly*; Q_t is the projection of P_t on the circle that circumscribes the orbit. Right panel: demonstration of the relation (A26) between the planetocentric orbital longitude of the star, $\lambda_\star$, the true anomaly, ν, and the argument of the pericenter, ω. The line of nodes is the intersection between the orbital plane and the equatorial plane of the planet; P_0 is the planet at the ascending node. For each position of the planet we show the instant direction of the lines of nodes, γ.

are $q(r)$ and $\delta_\star$. To calculate the seasonal evolution of $q(r)$ and $\delta_\star$ we proceed as follows.

We specify the position of the planet on its orbit using a system of polar coordinates centered on the star and origin of the angles in the direction to the pericenter, as shown in Figure 12. The position of the planet at time t, P_t, is specified by $r = r(t)$ and the *true anomaly*, $\nu = \nu(t)$. The instant stellar flux is given by $q(r) = (q_0/(r/a)^2)$ where $q_0 = L_\star/(4\pi a^2)$. The instantaneous value of r/a can be calculated by introducing an additional angular variable E (the *eccentric anomaly*) such that

$$r/a = 1 - e \cos E, \qquad (A24)$$

where e is the eccentricity and E is interpreted geometrically in the left panel of Figure 12. We show below how to compute E.

To calculate the stellar declination $\delta_\star$ we consider the *planetocentric orbital longitude of the star*, $\lambda_\star$, shown in the right panel of Figure 12. The origin of this angle is the line of nodes, defined by the intersection of the orbital plane with the equatorial plane. Without loss of generality, we set $t = 0$ the instant in which the planet crosses the ascending node.[5] With this choice, the instant value of the stellar declination is (Allison & McEwen 2000)

$$\delta_\star = \arcsin(\sin \varepsilon \, \sin \lambda_\star), \qquad (A25)$$

where ε is the obliquity, i.e., the inclination of the planet's orbit to its equator. To calculate $\lambda_\star(t)$ we consider its relation with the true anomaly, ν. From the top panel of Figure 12, it is easy to see that

$$\lambda_\star(t) = \nu(t) + \lambda_P, \qquad (A26)$$

where λ_P is the planetocentric longitude of the star at the moment in which the planet is at the pericenter (P_1 in the figure); in terms of orbital parameters, $\lambda_P = \omega$, where ω is the *argument of the*

pericenter. To solve Equation (A26), we use the expression (Bertotti & Farinella 1990, Equation (10.30), p. 211)

$$\tan(\nu/2) = \left(\frac{1 + e}{1 - e}\right)^{1/2} \tan(E/2) \qquad (A27)$$

that can be inferred from the top panel of Figure 12.

At this point we are left with the calculation of the eccentric anomaly E. To this end we use Kepler's equation

$$E - e \sin E = M, \qquad (A28)$$

where M is the *mean anomaly*, defined to be a linear function of time which increases by 2π per revolution according to the expression

$$M = \bar{n} t + M_\circ, \qquad (A29)$$

where $\bar{n} = 2\pi/P$. The constant M_0 is determined by the choice of the initial conditions. To solve the transcendent Kepler's equation (A28), we use Newton's iteration method.[6]

A.6. Zonal Coverage of Oceans, Land, Ice, and Clouds

The zonal ocean fraction, f_o, is a free parameter that also determines the fraction of continents $f_l = 1 - f_o$. By assigning f_o and f_l to each latitude zone of the planet, the EBM takes into account the planet geography, although in a schematic way.

The zonal coverage of ices, f_i, is calculated as a function of the mean diurnal zonal temperature, T. This approach, adopted by WK97 and followed by SM08, allows to incorporate the climate feedback between temperature and ice albedo into the EBM. In their original formulation, WK97 used data from Thompson & Barron (1981) to calculate the ocean fraction covered by sea ice as

$$f_i(T) = \max\{0, [1 - e^{(T - 273\,\mathrm{K})/10\,\mathrm{K}}]\}. \qquad (A30)$$

---

[5] The intersection of the orbital plane with a reference plane used to measure the orbit inclination is called the "lines of nodes." Here the adopted reference plane is the equatorial plane and the inclination coincides with the axis obliquity. The planet orbit intersects the lines of nodes in two points, called the ascending and descending nodes. The ascending node is the one in which $d(\delta_\star)/dt > 0$.

[6] Newton's method is based on the iteration $x_{i+1} = x_i - f(x_i)/f'(x_i)$. In practice, in our case $f(x) = E - e \sin E - M$ and therefore

$$E_{i+1} = E_i - \frac{E_i - e \sin E_i - M}{1 - e \cos E_i}.$$

This expression provides a "freezing curve" that ideally describes the formation of ices as the temperature decreases. However, in this formulation the ice melts completely and instantaneously as soon as $T > 273$ K. This approximation is too crude for zones that are frozen for most of the time: in such regions we expect a buildup of permanent ices if the timescales for ice formation and ice melting are comparable. To avoid this problem, we compare the time intervals in which $T < 273$ K and $T \geqslant 273$ K in each zone. If $T < 273$ K during more than 50% of the orbital period, we adopt a constant ice coverage for the full orbit, $f_i = f_i(\overline{T})$, where $\overline{T}$ is the mean *annual* zonal temperature. In the other cases, we follow the original formulation (A30). In this way we obtain the formation of permanent ices, with a coverage that increases as the mean zonal annual temperature decreases. Our treatment significantly improves the description of the ice coverage on Earth, avoiding a sudden appearance and disappearance of the polar caps in the course of each orbit. To keep the model simple, we adopt for the continents the same ice coverage of the oceans. A more realistic treatment of the ice coverage would require a formulation of the formation and melting of ices as a function of time. The dynamical treatment of the ice formation and melting is beyond the purpose of this paper and will be the subject of subsequent work. We refer to Spiegel et al. (2010) for a detailed discussion of ice formation and melting using an EBM.

As far as the cloud coverage is concerned, we adopt different values for clouds over oceans, continents, and ices in our formulation of the albedo (Equation (A13)). The observational support for variations of the cloud coverage on different types of underlying surfaces comes from an analysis of Earth data performed by Sanromá & Pallé (2012). These authors used data collected by the International Satellite Cloud Climatology Project and presented the cloud coverage as a function of latitude for clouds on water, ice, desert, and vegetation. We averaged these latitude profiles to obtain a global representative cloud coverage for each type of surface. The value for the water was slightly adjusted to improve the agreement of our model with the experimental albedo–latitude profiles of Earth. The cloud coverage over continents was calculated by weighting deserts and vegetation with factors 2/3 and 1/3, respectively.[7] As a result, we adopt $f_{cw} = 0.67$, $f_{cl} = 0.50$, and $f_{ci} = 0.50$ for clouds over water, continents, and ices, respectively. With this choice of parameters, we obtain a global cloud coverage $\langle f_c \rangle = 0.612$ in our best model for Earth. This value is in agreement with the experimental value $\langle f_c \rangle = 0.603$ obtained from the ERA Interim reanalysis for the years 1979–2010 (Dee et al. 2011). For comparison, WK97 adopted $\langle f_c \rangle = 0.5$ in their formulation of the surface albedo of Earth. An interesting feature of our formalism is that the cloud coverage is automatically adjusted for planets with different fractions of continents, oceans, and ices.

REFERENCES

Allison, M., & McEwen, M. 2000, P&SS, 48, 215
Anglada-Escudé, G., Arriagada, P., Vogt, S. S., et al. 2012, ApJL, 751, L16
Bartik, K., Bruylants, G., Locci, E., & Reisse, J. 2011, in Origins and Evolution of Life: An Astrobiological Perspective, ed. M. Gargaud, et al. (Cambridge: Cambridge Univ. Press), 205
Bertotti, B., & Farinella, P. 1990, Physics of the Earth and the Solar System (Dordrecht: Kluwer)
Borucki, W. J., Koch, D. G., Batalha, N., et al. 2012, ApJ, 745, 120
Briegleb, B. P., Minnis, P., Ramanathan, V., & Harrison, E. 1986, JCAM, 25, 214
Caballero, R. 2012, CliMT: An Object-oriented Climate Modeling and Diagnostics Toolkit, http://people.su.se/~rcaba/climt
Cavicchioli, R. 2002, AsBio, 2, 281
Cess, R. D. 1976, JAtS, 33, 1831
Dee, D. P., Uppala, S. M., Simmons, A. J., et al. 2011, QJRMS, 137, 553
Dole, S. H. 1964, Habitable Planets for Man (New York: Blaisdell Pub. Co.)
Dressing, C. D., Spiegel, D. S., Scharf, C. A., Menou, K., & Raymond, S. N. 2010, ApJ, 721, 1295
Enomoto, T. 2007, JAMSTEC Report of Research and Development, 6, 21
Forgan, D. 2012, MNRAS, 422, 1241
Gaidos, E., & Williams, D. M. 2004, NewA, 10, 67
Hart, M. H. 1979, Icar, 37, 351
Heller, R., & Barnes, R. 2013, AsBio, 13, 18
Heng, K., & Vogt, S. S. 2011, MNRAS, 415, 2145
Howard, A. W., Marcy, G. W., Bryson, S. T., et al. 2012, ApJS, 201, 15
Joshi, M. 2003, AsBio, 3, 415
Kasting, J. F., & Catling, D. 2003, ARA&A, 41, 429
Kasting, J. F., Whitmire, D. P., & Reynolds, R. T. 1993, Icar, 101, 108
Kiehl, J. T., & Briegleb, B. P. 1992, JGR, 97, 10037
Kite, E. S., Gaidos, E., & Manga, M. 2011, ApJ, 743, 41
Kondratyev, K. Y. A. (ed.) 1969, Radiation in the Atmosphere (New York: Academic)
Kopp, G., & Lean, J. L. 2011, GeoRL, 38, L01706
Lammer, H., Bredehöft, J. H., Coustenis, A., et al. 2009, A&ARv, 17, 181
Latham, D. W., Rowe, J. F., Quinn, S. N., et al. 2011, ApJL, 732, L24
Lide, D. R. 1997, CRC Handbook of Chemistry and Physics (Boca Raton, FL: CRC Press)
Lissauer, J. J., Ragozzine, D., Fabrycky, D. C., et al. 2011, ApJS, 197, 8
Lo Curto, G., Mayor, M., Benz, W., et al. 2010, A&A, 512, A48
Mayor, M., & Queloz, D. 1995, Natur, 378, 355
McGuffie, K., & Henderson-Sellers, A. 2005, A Climate Modelling Primer (3rd ed.; Chichester: Wiley)
Mordasini, C., Alibert, Y., Benz, W., Klahr, H., & Henning, T. 2012, A&A, 541, 97
North, G. R., & Coakley, J. A. 1979, JAtS, 36, 1189
North, G. R., Mengel, J. G., & Short, D. A. 1983, JGR, 88, 6576
Pepe, F., Lovis, C., Ségransan, D., et al. 2011, A&A, 534, 58
Pierrehumbert, R. T. 2010, Principles of Planetary Climate (Cambridge: Cambridge Univ. Press)
Pierrehumbert, R. T. 2011, ApJL, 726, L8
Pierrehumbert, R. T., & Gaidos, E. 2011, ApJL, 734, L13
Press, W. H., Flannery, B. P., Teukolsky, S. A., & Vetterling, W. T. 1992, Numerical Recipes in Fortran 77: The Art of Scientific Computing (Cambridge: Cambridge Univ. Press)
Reynolds, R. T., McKay, C. P., & Kasting, J. F. 1987, AdSpR, 7, 125
Salby, M. L. 2012, Physics of the Atmosphere and Climate (New York: Cambridge Univ. Press)
Sanromá, E., & Pallé, E. 2012, ApJ, 744, 188
Scharf, C. A. 2006, ApJ, 648, 1196
Selsis, F., Kasting, J. F., Paillet, J., & Delfosse, X. 2007, A&A, 476, 1373
Spiegel, D. S., Menou, K., & Scharf, C. A. 2008, ApJ, 681, 1609 (SMS08)
Spiegel, D. S., Menou, K., & Scharf, C. A. 2009, ApJ, 691, 596 (SMS09)
Spiegel, D. S., Raymond, S. N., Dressing, C. D., Scharf, C. A., & Mitchell, J. L. 2010, ApJ, 721, 1308
Thompson, S. L., & Barron, E. J. 1981, JG, 89, 143
Tuomi, M., Anglada-Escudé, G., Gerlach, E., et al. 2013, A&A, 549, 48
Udry, S., & Santos, N. C. 2007, ARA&A, 45, 397
Walker, J. C. G., Hays, P. B., & Kasting, J. F. 1981, JGR, 86, 9776
Williams, D. M., & Kasting, J. F. 1997, Icar, 129, 254 (WK97)
Williams, D. M., Kasting, J. F., & Wade, R. A. 1997, Natur, 385, 234
Williams, D. M., & Pollard, D. 2002, IJAsB, 1, 61
Wordsworth, R. D., Forget, F., Selsis, F., et al. 2011, ApJL, 733, L48

[7] http://phl.upr.edu/library/notes/vegetationiceanddesertsofthepaleo-earth.